Scotogenic model with U(1) symmetry and a scalar dark matter

Anjan Kumar Barik[1,*] Najimuddin Khan[2,†] and Santosh Kumar Rai[1,‡]

[1]*Regional Centre for Accelerator-based Particle Physics, Harish-Chandra Research Institute, A CI of Homi Bhabha National Institute, Chhatnag Road, Jhunsi, Prayagraj 211019, India*

[2]*Department of Physics, Aligarh Muslim University, Aligarh 202001, India*

(Received 5 July 2024; accepted 31 March 2025; published 22 April 2025)

We study a scotogenic model augmented with an additional $U(1)$ gauge and a discrete Z_2 symmetry. The lightest Z_2-odd particle in our model becomes the dark matter (DM) candidate while tiny neutrino masses are realized at one loop. We explore the parameter space of the model for which the DM relic density is satisfied, and the correct low-energy neutrino observables are reproduced. The extended gauge symmetry includes a beyond Standard Model (SM) particle spectrum consisting of vectorlike fermions and scalars. We also highlight possible collider signatures of these particles at the LHC.

DOI: 10.1103/PhysRevD.111.075023

I. INTRODUCTION

The modern era of particle physics has witnessed a remarkable period of success with the development and establishment of the Standard Model (SM). The discovery of a ~125 GeV Higgs at ATLAS [1] and CMS [2] completed the search for the particle spectrum of the SM. Although the SM of particle physics is a highly successful theoretical framework, it has some limitations as it cannot give any prediction of the DM present in the Universe, where it came from, and its nature. Neither can it explain the matter-antimatter asymmetry in the Universe, so pertinent to our very existence. Then there is the matter of gauge hierarchy problem that suggests the existence of some new physics not far above the electroweak scale and the nonzero mass of the neutrinos where SM falls short of expectations. These shortcomings motivate us to explore new theoretical ideas and their experimental investigations beyond the SM. Various astrophysical observations, such as Coma cluster [3], the gravitational lensing effects observed in the bullet cluster [4] and anomalies in galactic rotation curves [5,6], have provided compelling evidence for the existence of DM in the Universe. These observations indicate that there is additional mass in the Universe that does not interact with electromagnetic radiation and cannot be accounted for by the particles described within the SM of particle physics. In the SM of particle physics, neutrinos were originally assumed to be massless. However, experimental observations of neutrino oscillations have conclusively demonstrated that neutrinos have nonzero masses [7,8], which has motivated the need for extensions to the SM of particle physics. It is to be noted that neutrinos and DM have distinct properties and behaviors.

We study a scotogenic model, which is augmented with an additional $U(1)$ gauge symmetry. The success of the Standard Model being a gauge theory motivates us to consider BSM particles to be charged under certain gauge groups. The motivation for $U(1)$ gauge symmetry comes from grand unified theories (GUT), which contains the SM gauge group and has a rank greater than four. The mathematical fact that any theory with $SU(N)$ gauge symmetry, when spontaneously broken by a scalar in the adjoint representation, has its $N-1$ diagonal generators unbroken, therefore the theory has at least $U(1)^{N-1}$ symmetry [9]. In special cases when more than one real component of a scalar multiplet which breaks the $SU(N)$ gauge symmetry becomes equal, there will be a remnant non-Abelian gauge symmetry, e.g., $SO(10)$ and E_6 GUT have gauge symmetry of rank 5 and 6 respectively after symmetry breaking will give SM gauge group along with additional $U(1)$ symmetry.

In the $U(1)$ extension of SM, the new Abelian gauge boson can be a messenger between SM and BSM particles, even if the SM particles are neutral under the additional symmetry as the interactions can proceed via gauge kinetic mixing (GKM) between the SM $U(1)_Y$ and new $U(1)$ gauge bosons. The $U(1)$ extended BSM models can solve many phenomenological problems, e.g., μ problem in the MSSM (minimal supersymmetric SM) by dynamically generating the μ term, some flavor nonuniversal coupling of new gauge boson to lepton and quark sector can induce

*Contact author: anjanbarik@hri.res.in
†Contact author: nkhan.ph@amu.ac.in
‡Contact author: skr@hri.res.in

flavor violating loop decay, e.g., $\mu \to e\gamma$, $b \to s\gamma$ and also can contribute to the anomalous magnetic moment of the respective particle. $U(1)$ extension of SM can also explain neutrino mass, DM, matter-antimatter asymmetry of the universe etc. [9–14].

However, introducing additional particles and new symmetries into the SM comes with constraints on their masses and interactions with SM particles, as there is no convincing experimental evidence of their existence. Introduction of a new gauge boson, (Z') would also have to comply with various constraints such as the $Z-Z'$ mixing angle, its direct search limits at colliders, etc. While the precise measurement of the well-established Z decay widths to SM modes must remain within experimental errors [15], Z' search in Drell-Yan processes at LHC [16–18] put strong limits on its mass. To circumvent these limitations, we adopt a strategy where SM particles remain neutral under the new gauge symmetry, interacting with the Z' solely through the GKM. By maintaining a small GKM, we can effectively avoid these experimental constraints.

In this work, we have extended the SM by a $U(1)$ gauge symmetry with the inclusion of additional Z_2 symmetry. All the BSM particles are charged under the new gauge symmetry. In the Z_2 even sector along with SM particles, we have one gauge singlet scalar, which is responsible for breaking the new $U(1)$ gauge symmetry spontaneously. In the Z_2 odd sector, we have $SU(2)$ singlet and doublet scalar fields including vectorlike singlet and doublet fermions. We propose a scalar DM by making one of the CP-even scalars to be lightest among the Z_2 odd sector particles. Subsequently, we investigate the phenomenology of the DM being a $SU(2)$ singlet, doublet, and linear combination of both. By studying the DM phenomenology in the above scenarios, we aim to understand the model's viability in explaining the observed DM abundance in the Universe and to predict potential signals that can be probed experimentally. In addition, we thoroughly investigate relevant experimental and theoretical constraints on the model parameters. By considering these constraints, we can identify parameter space regions consistent with all available experimental data and gain insight into the model's overall viability and implications for DM phenomenology.

In the singlet and doublet dark matter radiative seesaw scenario, the dark matter relic density can be achieved near the Higgs resonance or in the mass region above 600 GeV. However, most parameter space is constrained by limits from the Higgs decay width and direct detection experiments. Moreover, neutrino physics imposes additional restrictions on the available parameter space. Our model has successfully accounted for nearly all possible ranges of dark matter masses that satisfy theoretical and experimental constraints. Furthermore, we have accurately described the low-energy neutrino observables for both normal and inverted mass hierarchies. To the best of our knowledge, these results have not been comprehensively addressed in previous radiative seesaw models.

The paper is organized as follows: Section II provides a concise overview of the $U(1)$ extended neutrino DM model. Section III is dedicated to discussing the relevant theoretical and experimental constraints associated with the model. Moving on to Sec. IV, we present the numerical analysis carried out to explore the model parameters in the context of neutrino and DM in depth. We discuss the possible collider search channels at the LHC in Sec. V. Finally, Sec. VI summarizes the key findings and draw conclusions based on our study.

II. MODEL

In the proposed model the SM gauge sector is extended by an Abelian $U(1)$ gauge symmetry. The model also contains new fields that carry charges under both the SM gauge group and the new $U(1)$. A discrete Z_2 symmetry is also included which is responsible for making the lightest particle odd under this symmetry to act as the DM of the Universe. The new particles and their corresponding charge assignment are shown in Table I. The scalar sector of the SM is extended to include a new doublet (Φ_2) and two complex singlet fields (S_1, S_2) while the fermion sector has a new vectorlike doublet (ψ) and singlet fermion (N). The model provides an explanation for neutrino mass via a radiative seesaw mechanism [19] while also providing a viable DM candidate.

A. Scalars

The model contains a new Z_2-odd $SU(2)$ Higgs doublet (Φ_2) and two complex scalar singlets $(S_1,\ S_2)$ where S_1 is Z_2-even while S_2 is Z_2-odd, in addition to the SM Higgs doublet (Φ_1). The kinetic part of the Lagrangian density for the above-mentioned scalars is given by,

$$\mathcal{L}_{KE} = \sum_{\phi} (D_\mu \phi)^\dagger (D^\mu \phi), \tag{1}$$

where $\phi = \Phi_1, \Phi_2, S_1, S_2$ and D_μ represents the covariant derivatives given by,

TABLE I. Additional particle content and their charge assignments under symmetry groups.

Particles	$\psi = (N_D, E_1^-)^T$	N	Φ_2	S_1	S_2
$SU(2)_L$	2	1	2	1	1
$U(1)_Y$	−1	0	1	0	0
$U(1)_X$	1	1	1	2	1
Z_2	−1	−1	−1	1	−1

$$D_\mu^{\Phi_1} = \partial_\mu - i\frac{g_2}{2}\sigma^a.W_\mu^a - i\frac{g_1}{2}YB_\mu$$
$$D_\mu^{\Phi_2} = \partial_\mu - i\frac{g_2}{2}\sigma^a.W_\mu^a - i\frac{g_1}{2}YB_\mu - i\frac{g_x}{2}XC_\mu$$
$$D_\mu^{S_{1,2}} = \partial_\mu - i\frac{g_x}{2}XC_\mu \tag{2}$$

where σ^a are the Pauli matrices and W_μ^a are the $SU(2)_L$ gauge bosons ($a = 1, 2, 3$). The B_μ and C_μ are the $U(1)_Y$ and $U(1)_X$ gauge bosons, respectively. The gauge-invariant scalar potential in the Lagrangian is,

$$\mathcal{V} = V_1 + V_2 + V_{12}, \tag{3}$$

where,

$$V_1 = -\mu_{\phi_1}^2\Phi_1^\dagger\Phi_1 - \mu_{S_1}^2 S_1^\dagger S_1 + \lambda_1(\Phi_1^\dagger\Phi_1)^2 + \lambda_{11}\Phi_1^\dagger\Phi_1 S_1^\dagger S_1 + \lambda_{s1}(S_1^\dagger S_1)^2$$
$$V_2 = \mu_{\phi_2}^2\Phi_2^\dagger\Phi_2 + \mu_{\phi_{s2}}^2 S_2^\dagger S_2 + \lambda_2(\Phi_2^\dagger\Phi_2)^2 + \lambda_{22}\Phi_2^\dagger\Phi_2 S_2^\dagger S_2 + \lambda_{s2}(S_2^\dagger S_2)^2$$
$$V_{12} = \lambda_3\Phi_1^\dagger\Phi_1\Phi_2^\dagger\Phi_2 + \lambda_4\Phi_1^\dagger\Phi_2\Phi_2^\dagger\Phi_1 + \kappa_1\Phi_1^\dagger\Phi_1 S_2^\dagger S_2 + \kappa_2\Phi_2^\dagger\Phi_2 S_1^\dagger S_1$$
$$+ \kappa_3 S_1^\dagger S_1 S_2^\dagger S_2 + (\kappa_4\Phi_2^\dagger\Phi_1 S_2^\dagger S_1 - \sqrt{2}\mu_S S_2^{\dagger 2} S_1 + \mu_h\Phi_2^\dagger\Phi_1 S_2 + \text{H.c.}). \tag{4}$$

In the above potential, the μ's are the bare masses of the scalars while the λ's and κ's are the quartic couplings. Among the two Higgs doublets only the Φ_1 gets a vacuum expectation value (VEV) and is responsible for the electroweak symmetry breaking (EWSB) of $SU(2)_L \times U(1)_Y \to U(1)_{em}$. Similarly, the Z_2-even SM singlet scalar (S_1) gets a VEV and is responsible for the breaking of the $U(1)_X$ gauge symmetry. The scalars can now be written in their explicit component form as,

$$\Phi_1 = \begin{pmatrix} G^+ \\ \frac{(\phi_{dr1}+v_1+iG^0)}{\sqrt{2}} \end{pmatrix}; \qquad \Phi_2 = \begin{pmatrix} H^+ \\ \frac{(\phi_{dr2}+i\phi_{di2})}{\sqrt{2}} \end{pmatrix}.$$

and

$$S_1 = \frac{(\phi_{sr1} + v_s + i\phi_{si1})}{\sqrt{2}}; \qquad S_2 = \frac{(\phi_{sr2} + i\phi_{si2})}{\sqrt{2}}.$$

The minimization conditions for the potential are,

$$\mu_{\phi_1}^2 = \frac{1}{2}(\lambda_{11}v_s^2 + 2\lambda_1 v_1^2), \quad \mu_{S_1}^2 = \frac{1}{2}(2\lambda_{s1}v_s^2 + \lambda_{11}v_1^2) \tag{5}$$

The CP-even components, (ϕ_{dr1} and ϕ_{sr1}) mix after EWSB. Using the minimization conditions, we can write the mass matrix in the (ϕ_{dr1}, ϕ_{sr1}) basis as,

$$(\phi_{dr1}\phi_{sr1})\begin{pmatrix} \mathcal{M}_{a11} & \mathcal{M}_{a12} \\ \mathcal{M}_{a21} & \mathcal{M}_{a22} \end{pmatrix}\begin{pmatrix} \phi_{dr1} \\ \phi_{sr1} \end{pmatrix}, \tag{6}$$

where, $\mathcal{M}_{a11} = 2\lambda_1 v_1^2, \mathcal{M}_{a22} = 2\lambda_{s1}v_s^2$ and $\mathcal{M}_{a12} = \mathcal{M}_{a21} = \lambda_{11}v_1 v_s$. The mass eigenstates are obtained by diagonalizing the mass matrix in Eq. (6) with a rotation of the $(\phi_{dr1}\phi_{sr1})$ basis as,

$$\begin{pmatrix} h \\ H \end{pmatrix} = Z_H\begin{pmatrix} \phi_{dr1} \\ \phi_{sr1} \end{pmatrix}, \text{ with } Z_H = \begin{pmatrix} \cos\alpha & -\sin\alpha \\ \sin\alpha & \cos\alpha \end{pmatrix} \tag{7}$$

The mixing angle α between the CP-even scalars is given by,

$$\alpha = \frac{1}{2}\arctan\left(\frac{2\mathcal{M}_{a12}}{\mathcal{M}_{a22} - \mathcal{M}_{a11}}\right) \tag{8}$$

The masses of the scalars are,

$$M_h^2 = \frac{1}{2}\left[(\mathcal{M}_{a22} + \mathcal{M}_{a11}) - \sqrt{(\mathcal{M}_{a22} - \mathcal{M}_{a11})^2 + 4\mathcal{M}_{a12}^2}\right]$$
$$M_H^2 = \frac{1}{2}\left[(\mathcal{M}_{a22} + \mathcal{M}_{a11}) + \sqrt{(\mathcal{M}_{a22} - \mathcal{M}_{a11})^2 + 4\mathcal{M}_{a12}^2}\right] \tag{9}$$

Here h is considered to be the observed SM-like Higgs boson with mass $m_h \simeq 125$ GeV and H is a heavy scalar. The couplings of the h to the known fermions and gauge bosons get modified depending on the mixing. The CP-odd scalars of Φ_1 and S_1 become the Goldstone bosons and get absorbed to give mass to the neutral gauge bosons, while the charged component of Φ_1 is absorbed by the $W^\pm$ boson.

The charged component $\phi_{d2}^\pm \equiv H^\pm$ of the Z_2 odd doublet does not mix with the other scalar fields and its mass is given by,

$$M_{H^\pm}^2 = \mu_{\phi_2}^2 + \frac{1}{2}\kappa_1 v_s^2 + \frac{1}{2}\lambda_3 v_1^2 \tag{10}$$

The CP-even part of the scalar fields ϕ_{dr2} and ϕ_{sr2} from the Z_2-odd sector also mix. The masses are given by,

$$M_{H_1}^2 = \frac{1}{2}\left[(\mathcal{M}_{b22} + \mathcal{M}_{b11}) - \sqrt{(\mathcal{M}_{b22} - \mathcal{M}_{b11})^2 + 4\mathcal{M}_{b12}^2}\right]$$
$$M_{H_2}^2 = \frac{1}{2}\left[(\mathcal{M}_{b22} + \mathcal{M}_{b11}) + \sqrt{(\mathcal{M}_{b22} - \mathcal{M}_{b11})^2 + 4\mathcal{M}_{b12}^2}\right], \tag{11}$$

with mixing angle β, where $\beta = \frac{1}{2}\arctan((2\mathcal{M}_{b12})/(\mathcal{M}_{b22} - \mathcal{M}_{b11}))$. Similarly, the masses of the Z_2-odd pseudoscalar fields are,

$$M_{A_1}^2 = \frac{1}{2}\left[(\mathcal{M}_{b22} + 4\mu_S v_s + \mathcal{M}_{b11}) - \sqrt{(\mathcal{M}_{b22} + 4\mu_S v_s - \mathcal{M}_{b11})^2 + 4\mathcal{M}_{b12}^2}\right]$$
$$M_{A_2}^2 = \frac{1}{2}\left[(\mathcal{M}_{b22} + 4\mu_S v_s + \mathcal{M}_{b11}) + \sqrt{(\mathcal{M}_{b22} + 4\mu_S v_s - \mathcal{M}_{b11})^2 + 4\mathcal{M}_{b12}^2}\right], \quad (12)$$

where,

$$\mathcal{M}_{b11} = M_{H^\pm}^2 + \frac{1}{2}\lambda_4 v_1^2, \qquad \mathcal{M}_{b12} = \mathcal{M}_{b21} = \mu_h v_1 + \frac{1}{2}\kappa_4 v_1 v_s$$
$$\mathcal{M}_{b22} = \mu_{\phi_{2s}}^2 - 2\mu_S v_s + \frac{1}{2}\kappa_3 v_s^2 + \frac{1}{2}\kappa_2 v_1^2 \quad (13)$$

It is to be noted that the mixing angle in the CP-odd sector (δ) is different than the mixing angle in the CP-even sector (β) due to the presence of an additional term $4\mu_S v_s$ in the '22' component of the mass matrix. The other terms are same as in Eq. (13). The CP-odd scalar mixing angle δ can be related with β as,

$$\frac{1}{\tan 2\delta} = \frac{1}{\tan 2\beta} + \frac{4\mu_S v_s}{2\mathcal{M}_{b12}}, \quad (14)$$

B. Gauge bosons

The model has the SM gauge bosons and an additional neutral gauge boson because of the new $U(1)_X$ gauge symmetry. As the field strength tensor of an Abelian gauge field is gauge invariant, we can write a cross term involving the field strength tensors of the two different $U(1)$ gauge fields [20,21]. The kinetic term representing all the gauge fields in the model can be written as,

$$\mathcal{L} \supset -\frac{1}{4}G^{a,\mu\nu}G^a_{\mu\nu} - \frac{1}{4}W^{b,\mu\nu}W^b_{\mu\nu} - \frac{1}{4}B^{\mu\nu}B_{\mu\nu} - \frac{1}{4}C^{\mu\nu}C_{\mu\nu} + \frac{1}{2}\tilde{g}B^{\mu\nu}C_{\mu\nu}. \quad (15)$$

Where, $G^{a,\mu\nu}$, $W^{b,\mu\nu}$, $B^{\mu\nu}$, and $C_{\mu\nu}$ are field strength tensor for $SU(3)$, $SU(2)$, $U(1)_Y$, and $U(1)_X$ gauge bosons respectively.

We redefine the two Abelian gauge fields so that, the kinetic term will be diagonal.

$$B^\mu = B'^\mu + \frac{\tilde{g}}{\sqrt{1-\tilde{g}^2}}C'^\mu, \qquad C^\mu = \frac{1}{\sqrt{1-\tilde{g}^2}}C'^\mu. \quad (16)$$

After spontaneous symmetry breaking, the gauge bosons corresponding to the broken symmetry become massive. The mass term of the gauge bosons can be obtained from the kinetic part of the Z_2-even scalar sector as follows,

$$\mathcal{L}_{m,\text{gauge}} = \frac{1}{4}\left|\begin{pmatrix} g_2 W_\mu^3 - g_1 B_\mu & g_2(W_\mu^1 - iW_\mu^2) \\ g_2(W_\mu^1 + iW_\mu^2) & -g_2 W_\mu^3 - g_1 B_\mu \end{pmatrix}\begin{pmatrix} 0 \\ \frac{v_1}{\sqrt{2}} \end{pmatrix}\right|^2 + \frac{1}{2}g_x^2 v_s^2 C_\mu C^\mu$$
$$= \frac{1}{4}g_2^2 v^2 W_\mu^+ W^{-\mu} + \frac{1}{8}v_1^2\left|\left(g_2 W_\mu^3 - g_1 B'_\mu - \frac{g_1\tilde{g}}{\sqrt{1-\tilde{g}^2}}C'_\mu\right)\right|^2 + \frac{g_x^2 v_s^2}{2(1-\tilde{g}^2)}C'_\mu C'^\mu.$$

We make the following redefinition of parameters to get a simple expression for the gauge boson mass matrix,

$$g'_x = \frac{g_1\tilde{g}}{\sqrt{1-\tilde{g}^2}}, \qquad \frac{g_x}{\sqrt{1-\tilde{g}^2}} \to g_x. \quad (17)$$

From the above Lagrangian, the mass matrix for the neutral gauge bosons, in the basis of $(B'_\mu W_\mu^3 C'_\mu)^T$ is given by,

$$M^2 = \frac{1}{4}\begin{pmatrix} g_1^2 v^2 & -g_1 g_2 v^2 & g_1 g'_x v^2 \\ -g_1 g_2 v^2 & g_2^2 v^2 & -g_2 g'_x v^2 \\ g_1 g'_x v^2 & -g_2 g'_x v^2 & g_x'^2 v^2 + 4g_x^2 v_s^2 \end{pmatrix}. \quad (18)$$

For the diagonalization of the neutral gauge boson mass matrix, we first perform an orthogonal transformation in W_μ^3 and B'_μ plane.

$$\begin{pmatrix} A_\mu \\ X_\mu \\ C'_\mu \end{pmatrix} = \begin{pmatrix} \cos\theta_W & \sin\theta_W & 0 \\ -\sin\theta_W & \cos\theta_W & 0 \\ 0 & 0 & 1 \end{pmatrix} \begin{pmatrix} B'_\mu \\ W^3_\mu \\ C'_\mu \end{pmatrix}, \tag{19}$$

where $\tan\theta_W = \frac{g_1}{g_2}$. The mass term for neutral gauge bosons in the Lagrangian in the above rotated basis is given by,

$$\mathcal{L}_{m,\text{gauge}} = \frac{1}{8} v_1^2 (g_z X_\mu - g'_x C'_\mu)^2 + \frac{1}{2} g_x^2 v_s^2 C'_\mu C'^\mu, \tag{20}$$

where $g_z = \sqrt{g_1{}^2 + g_2^2}$. From the above Lagrangian, we find that there is no mass term for the A_μ field, which is the photon field and θ_W is the Weinberg angle. The mass matrix in X_μ and C'_μ basis is given by,

$$\tilde{M}^2 = \frac{1}{4} \begin{pmatrix} g_z^2 v^2 & -g_z g'_x v^2 \\ -g_z g'_x v^2 & g'^2_x v^2 + 4 g_x^2 v_s^2 \end{pmatrix}. \tag{21}$$

The above mass matrix can be diagonalized by the following orthogonal transformation,

$$\begin{pmatrix} Z_\mu \\ Z'_\mu \end{pmatrix} = \begin{pmatrix} \cos\theta' & \sin\theta' \\ -\sin\theta' & \cos\theta' \end{pmatrix} \begin{pmatrix} X_\mu \\ C'_\mu \end{pmatrix}, \tag{22}$$

where

$$\tan 2\theta' = \frac{2 g_z g'_x v^2}{g'^2_x v^2 + 4 g_x^2 v_s^2 - g_z^2 v^2}.$$

The final rotation matrix is given by,

$$\begin{pmatrix} B_\mu \\ W^3_\mu \\ C_\mu \end{pmatrix} = \begin{pmatrix} \cos\theta_W & -\sin\theta_W \cos\theta' + \frac{g'_x}{g_1}\sin\theta' & \sin\theta_W \sin\theta' + \frac{g'_x}{g_1}\cos\theta' \\ \sin\theta_W & \cos\theta_W \cos\theta' & -\cos\theta_W \sin\theta' \\ 0 & \sin\theta' \frac{\sqrt{g_1^2 + g_x^2}}{g_1} & \cos\theta' \frac{\sqrt{g_1^2 + g_x^2}}{g_1} \end{pmatrix} \begin{pmatrix} A_\mu \\ Z_\mu \\ Z'_\mu \end{pmatrix}.$$

The masses of the physical gauge bosons are,

$$M^2_{Z,Z'} = \frac{1}{8}[g_z^2 v^2 + g'_x v^2 + 4 g_x^2 v_s^2] \mp \frac{1}{8}\sqrt{(g'^2_x v^2 + g_z^2 v^2 + 4 g_x^2 v_s^2)^2 - 16 g_z^2 g_x^2 v^2 v_s^2}.$$

C. Fermions

As the SM fermions are neutral under the new gauge group, the Lagrangian for quarks remains unchanged while the SM leptons can have additional interaction with BSM fermions. The kinetic and interaction part for the newly added fermions is given by,

$$\begin{aligned} \mathcal{L} = {} & i\bar{\psi} \not{D}^\psi \psi + i\bar{N}_L \not{D}^N N_L + i\bar{N}_R \not{D}^N N_R + M_L \bar{\psi}\psi + M_N \bar{N}_L N_R \\ & + Y_{N_1} \bar{\psi}_L \Phi_1 N_R + Y_{N_2} \bar{\psi}_R \Phi_1 N_L + Y_{N_L} \bar{N}_L N_L^c S_1 + Y_{N_R} \bar{N}_R N_R^c S_1 \\ & + Y_{fd} \bar{\psi}_L \Phi_2 e_R + Y_{fx} \bar{\psi}_R S_2 \ell_L + Y_{f\nu} \overline{\ell}_L \tilde{\Phi}_2 N_R + \text{H.c.} \end{aligned} \tag{23}$$

When the SM Higgs gets VEV the singlet and doublet neutral BSM fermions mix with each other. Due to the presence of the Majorana mass term, there will be four Majorana fermions. The mass matrix of neutral BSM fermions, in the basis of $\psi^0 = (N_{DL}, N_{DR}^c, N_L, N_R^c)$ is given by,

$$\mathcal{M}^n = \begin{pmatrix} 0 & M_L & 0 & \frac{Y_{N_1} v_1}{\sqrt{2}} \\ M_L & 0 & \frac{Y_{N_2} v_1}{\sqrt{2}} & 0 \\ 0 & \frac{Y_{N_2} v_1}{\sqrt{2}} & \sqrt{2} Y_{N_L} v_s & M_N \\ \frac{Y_{N_1} v_1}{\sqrt{2}} & 0 & M_N & \sqrt{2} Y_{N_R} v_s \end{pmatrix} \tag{24}$$

This matrix can be diagonalized by the unitary (4×4) matrix $\mathcal{U}_N^{ij}$ with $i, j = 1, 2, 3, 4$. The new heavy fermionic state χ_i is given by,

$$\chi_i = \mathcal{U}_N^{ij} \psi_j^0 \tag{25}$$

For the choices of $Y_{N_1} = Y_{N_2}$ and $Y_{N_L} = Y_{N_R}$, we get the eigenvalues of the heavy neutrinos as,

$$M_{N_{i=1,2}} = \frac{Y_{N_R} v_s}{\sqrt{2}} + \frac{(M_L + M_N)}{2} \pm \frac{1}{2}\sqrt{2Y_{N_2}^2 v_1^2 + (\sqrt{2}Y_{N_R} v_s - M_L + M_N)^2}$$
$$M_{N_{i=3,4}} = \frac{Y_{N_R} v_s}{\sqrt{2}} - \frac{(M_L + M_N)}{2} \pm \frac{1}{2}\sqrt{2Y_{N_2}^2 v_1^2 + (\sqrt{2}Y_{N_R} v_s + M_L - M_N)^2}$$

The $\psi^{\pm}$ being a Z_2 odd charged fermion does not mix with SM leptons and is a Dirac fermion with mass M_L.

III. CONSTRAINTS ON THIS MODEL

The parameter space of our model is subject to various relevant constraints derived from theoretical considerations and observational phenomena. These constraints include absolute vacuum stability, unitarity of the scattering matrix, and the experimental searches for DM. In addition to these constraints, recent measurements of the Higgs invisible decay width and signal strength at the LHC impose further limitations on the parameter space.

By considering these additional constraints, we aim to refine our understanding of the viable parameter space for our model and further elucidate its implications for the observed phenomena. In the next section, we address these constraints.

A. Stability of the scalar potential

The scalar potential should be bounded from the below in such a way that, even for large field values, no other negative infinity arises along any field direction. Following the paper [22], the absolute stability condition for the potential in Eq. (3) are evaluated in terms of the quadratic couplings. The most stringent conditions are,

$$\begin{aligned}
&\lambda_1 \geq 0, \qquad \lambda_2 \geq 0, \qquad \lambda_{s1} \geq 0, \qquad \lambda_{s1} \geq 0,\\
&\lambda_3 \geq -2\sqrt{\lambda_1\lambda_2}, \qquad \lambda_3 + \lambda_4 \geq -2\sqrt{\lambda_1\lambda_2},\\
&\lambda_{11} \geq -2\sqrt{\lambda_1\lambda_{s2}}, \qquad \lambda_{22} \geq -2\sqrt{\lambda_2\lambda_{s2}},\\
&\kappa_{s_2\phi_1} \geq -2\sqrt{\lambda_1\lambda_{s2}}, \qquad \kappa_{s_1\phi_2} \geq -2\sqrt{\lambda_2\lambda_{s2}},\\
&\kappa_3 \geq -2\sqrt{\lambda_{s2}\lambda_{s2}}, \qquad \kappa_{s_2\phi_1} \geq -2\sqrt{\lambda_1\lambda_{s2}},
\end{aligned} \tag{26}$$

We also list the other stability conditions following [22] which are shown in Appendix VII.

B. Unitarity constraints

The unitarity bound on the extended scalar sectors can be calculated from the scalar-scalar, gauge boson-gauge boson, and scalar-gauge boson scattering matrix (S-matrix). The technique was developed in Refs. [23,24]. Using the Born approximation, the scattering cross section for any process is given by,

$$\sigma = \frac{16\pi}{s}\sum_{l=1}^{\infty}(2l+1)|a_l(s)|^2, \tag{27}$$

where, s is the Mandelstam variable and $a_l(s)$ are the partial wave coefficients corresponding to specific angular momenta l. This leads to the following unitarity constraint: $\mathrm{Re}[a_l(s)] < \frac{1}{2}$ [23,24]. At high energy, the dominant contribution to the amplitude $a_l(s)$ of the two-body scattering processes comes from the diagram involving the quartic couplings. Far from the resonance, the contributions from the heavy fields mediated s, t, u-channels are negligibly small. The equivalence theorem implies that, for $s \gg 1$ TeV, the amplitude of scattering processes involving longitudinal gauge bosons can be approximated by the scalar amplitude in which gauge bosons are replaced by their corresponding Goldstone bosons. So, to test the unitarity of these model parameters, we construct the S-matrix, which consists of only the scalar quartic couplings. Calculating the unitary bounds in the physical basis of the scalar fields is also challenging. The S-matrix, expressed in terms of physical fields, can be rotated into an S-matrix for the nonphysical fields (before the EWSB) by making a unitary transformation.

One can expand the potential in Eq. (3) and get various quartic couplings in nonphysical bases $\phi_{dr1}, \phi_{dr2}, \phi_{sr1}, \phi_{sr2}, \phi_{di1}(\equiv G^0), \phi_{di2}, \phi_{si1}, \phi_{si2}, \phi_{d1}^{\pm}(\equiv G^{\pm}), \phi_{d2}^{\pm},$. They are given in Appendix VII. The full set of all scattering processes can be expressed as a 40×40 S-matrix. This matrix is composed of three submatrices of dimensions 16×16, 14×14, and 10×10 which have different initial and final states. All the matrices are shown in the Appendix VII. The eigenvalues of these matrices are,

$$\lambda_{11}, \lambda_{22}, \lambda_3, 2\lambda_1, 2\lambda_2, 2\lambda_{s1}, 2\lambda_{s2}, \lambda_3 \pm \lambda_4, \lambda_3 + 2\lambda_4, \kappa_{s_2\phi_1}, \kappa_{s_1\phi_2}, \kappa_3, \lambda_1 + \lambda_2 \pm \sqrt{(\lambda_1 - \lambda_2)^2 + \lambda_4^2},$$
$$3\lambda_1 + 3\lambda_2 \pm \sqrt{9(\lambda_1 - \lambda_2)^2 + (2\lambda_3 + \lambda_4)^2}, 2\lambda_{s1} + 2\lambda_{s2} \pm \sqrt{\kappa_{s_1 s_2}^2 + 4(\lambda_{s1} - \lambda_{s2})^2}.$$

Throughout the analysis, we consistently apply the bounds imposed by the unitary constraints of scattering processes, which require the eigenvalues of the S-matrix to be less than or equal to 8π.

C. Constraints from electroweak precision experiments

New physics contributions beyond the electroweak scale have the potential to impact the electroweak precision bounds. These contributions primarily manifest through vacuum polarization corrections, which involve virtual particles in loop diagrams. These parameters were introduced and extensively studied in the works of Peskin and Takeuchi [25], Altarelli *et al.* [26], and Baak *et al.* [27]. The electroweak precision experiments utilize parameters known as S, T, and U to impose constraints on the new physics contributions. The S parameter characterizes new physics contributions to the neutral weak current, while the T parameter quantifies the contributions to the difference between the neutral and charged weak currents. On the other hand, the U parameter is solely sensitive to the mass and width of the W-boson. The contributions from beyond the BSM physics can arise from the presence of additional scalar and fermion doublets. One can add the new physics contributions to the SM as,

$$S = S_{\rm SM} + \Delta S_{SD} + \Delta S_{FD}, \qquad T = T_{\rm SM} + \Delta T_{SD} + \Delta T_{FD}, \qquad U = U_{\rm SM} + \Delta U_{SD} + \Delta U_{FD},$$

where, SD stands for scalar doublet whereas FD refers fermionic doublet contributions. The contribution from the Z_2-odd scalar doublet are given by,

$$\Delta S_{SD} = \frac{1}{2\pi}\left[\frac{1}{6}\ln\frac{M_{H_d}^2}{M_{H^\pm}^2} - \frac{5}{36} + \frac{M_{H_d}^2 M_{A_d}^2}{3(M_{A_d}^2 - M_{H_d}^2)^2} + \frac{M_A^4(M_{A_d}^2 - 3M_{H_d}^2)}{6(M_{A_d}^2 - M_{H_d}^2)^3}\ln\frac{M_{A_d}^2}{M_{H_d}^2}\right], \tag{28}$$

$$\Delta T_{SD} = \frac{1}{32\pi^2\alpha v^2}[F(M_{H^\pm}^2, M_{H_d}^2) + F(M_{H^\pm}^2, M_{A_d}^2) - F(M_{A_d}^2, M_{H_d}^2)]. \tag{29}$$

and ΔU_{SD} is neglected in this case due to small mass differences $M_{A_1} - M_{H_1}$ and $M_{H^\pm} - M_{H_1}$ of the inert fields [28,29]. The loop function

$$F(x,y) = \begin{cases} \frac{x+y}{2} - \frac{xy}{x-y}\ln\left(\frac{x}{y}\right) & x \neq y \\ 0 & x = y \end{cases}.$$

The fermionic contributions to S and T while considering the electric charge neutral BSM singlet and doublet fermions mixing is given by,

$$\begin{aligned}\pi\Delta S_{FD} = {} & \frac{1}{6} - 2b_2(M_L, M_L, 0) + \sum_{j,k=1}^{4}(|\mathcal{U}_{N_{1j}}|^2|\mathcal{U}_{N_{1k}}|^2 + |\mathcal{U}_{N_{2j}}|^2|\mathcal{U}_{N_{2k}}|^2)b_2(M_{N_j}, M_{N_k}, 0) \\ & + \sum_{j,k=1}^{4}\Re(\mathcal{U}_{N_{1j}}\mathcal{U}^*_{N_{1k}}\mathcal{U}_{N_{2j}}\mathcal{U}^*_{N_{2k}})f(M_{N_j}, M_{N_k})\end{aligned} \tag{30}$$

$$\begin{aligned}4\pi s_w^2 c_w^2 M_Z^2 \Delta T_{FD} = {} & -2\sum_{k=1}^{4}(|\mathcal{U}_{N_{1k}}|^2 + |\mathcal{U}_{N_{2k}}|^2)b_3(M_{N_k}, M_L, 0) + 2M_L^2 b_1(M_L, M_L, 0) \\ & + 2\sum_{k=1}^{4} M_L M_{N_k}\Re(\mathcal{U}_{N_{1k}}\mathcal{U}_{N_{2k}})b_0(M_L, M_{N_k}, 0) \\ & - \sum_{j,k=1}^{4}\Re(\mathcal{U}_{N_{1j}}\mathcal{U}^*_{N_{1k}}\mathcal{U}_{N_{2j}}\mathcal{U}^*_{N_{2k}})M_{N_j}M_{N_k}b_0(M_{N_j}, M_{N_k}, 0) \\ & + \sum_{j,k=1}^{4}(|\mathcal{U}_{N_{1j}}|^2|\mathcal{U}_{N_{1k}}|^2 + |\mathcal{U}_{N_{2j}}|^2|\mathcal{U}_{N_{2k}}|^2)b_3(M_{N_j}, M_{N_k}, 0),\end{aligned} \tag{31}$$

where

$$b_0(M_1,M_2,q^2) = \int_0^1 \log\left(\frac{\Delta}{\Lambda^2}\right)dx, \qquad b_1(M_1,M_2,q^2) = \int_0^1 x\log\left(\frac{\Delta}{\Lambda^2}\right)dx,$$
$$b_2(M_1,M_2,q^2) = \int_0^1 x(1-x)\log\left(\frac{\Delta}{\Lambda^2}\right)dx, \qquad b_3(M_1,M_2,0) = \frac{M_2^2 b_1(M_1,M_2,0) + M_1^2 b_1(M_1,M_2,0)}{2},$$
$$\Delta = M_2^2 x + M_1^2(1-x) - x(1-x)q^2, \tag{32}$$

Λ is the regularization scale, and

$$f(M_1,M_2) = M_1M_2\frac{M_2^4 - M_1^4 + 2M_1^2M_2^2\log(\frac{M_1^2}{\Lambda^2}) - 2M_1^2M_2^2\log(\frac{M_2^2}{\Lambda^2})}{2(M_1^2-M_2^2)^3}.$$

To impose constraints on the new parameters, we utilize the next-to-next-to-leading order (NNLO) global electroweak fit results obtained by the Gfitter group [30]. The results from their study provide significant limitations on the parameter space. The key constraints extracted from the fit [30] at 95% CL are,

$$\Delta S_{\rm BSM} < 0.04 \pm 0.11, \qquad T_{\rm BSM} < 0.09 \pm 0.14,$$
$$\Delta U_{\rm BSM} < -0.02 \pm 0.11.$$

In this model, we have checked that a small mass difference between the charged and neutral fermions of the doublet, with $M_{N_i} \geq 200$ GeV and a heavy singlet charged fermion mass of $\mathcal{O}(1)$ TeV, is considered to evade these constraints, i.e., the contributions from the new vectorlike fermions $\Delta S_{FD} \approx 0, \Delta T_{FD} \approx 0$ [31].

D. LHC signal strength constraints

In the presence of an additional Z_2-even scalar singlet (S_1), the tree-level couplings of a Higgs-like scalar h to SM fermions and gauge bosons undergo modifications due to the mixing. It leads to changes in the coupling strengths. Furthermore, the Higgs h loop-induced decays are also affected by the extra charged scalar ($H^\pm$) and fermion ($E_1^\pm$). The combined effects result in altered signal strength for the Higgs-like scalar h compared to its standard behavior. For the production cross section $\sigma(pp\to h)$ and decay width $h\to\chi$, we have,

$$\kappa_p^2 = \frac{\sigma(pp\to h)_{\rm BSM}}{\sigma(pp\to h)_{\rm SM}}, \qquad \kappa_\chi^2 = \frac{\Gamma(h\to\chi)_{\rm BSM}}{\Gamma(h\to\chi)_{\rm SM}}, \tag{33}$$

where χ stands for the final state $b\bar{b}, \tau^-\tau^+, W^-W^+, ZZ, Z\gamma$ and $\gamma\gamma$. It is possible to impose significant constraints on the scalar mixing from these channels. The most stringent constraints arise from the $Z\gamma$ and $\gamma\gamma$ channels. The safest bound on the mixing angle is $\cos\alpha > 0.995$ [32,33]. The loop-induced processes, mainly diphoton Higgs signal strength, put the most stringent constraints. The Higgs to diphoton strength, under the narrow width approximation, can be expressed as follows,

$$\mu_{\gamma\gamma} \approx \kappa_{\gamma\gamma}^2 = \frac{\sigma(gg\to h)_{\rm BSM}}{\sigma(gg\to h)_{\rm SM}}\frac{{\rm Br}(h\to\gamma\gamma)_{\rm BSM}}{{\rm Br}(h\to\gamma\gamma)_{\rm SM}}. \tag{34}$$

The production of the Higgs boson through gluons is much larger than the fermions. We can write $\frac{\sigma(gg\to h)_{\rm BSM}}{\sigma(gg\to h)_{\rm SM}} = \cos^2\alpha \approx 1$, hence,

$$\mu_{\gamma\gamma} = \frac{\Gamma_{\rm SM}^{\rm Total}}{\Gamma_{\rm BSM}^{\rm Total}}\frac{\Gamma(h\to\gamma\gamma)_{\rm BSM}}{\Gamma(h\to\gamma\gamma)_{\rm SM}}. \tag{35}$$

If the mass of the extra BSM particles is lighter than $\frac{M_h}{2}$, then it will contribute to the invisible decay width of the Higgs boson. We find that such an invisible allowed branching ratio is much less than 10% [34,35]. Hence, the ratio $\frac{\Gamma_{\rm SM}^{\rm Total}}{\Gamma_{\rm BSM}^{\rm Total}}$ could vary 0.9–1. However for new particle's masses $\frac{M_h}{2} >$, one can write $\frac{\Gamma_{\rm SM}^{\rm Total}}{\Gamma_{\rm BSM}^{\rm Total}} \approx \frac{1}{\cos^2\alpha} \approx 1$, hence, $\mu_{\gamma\gamma} = \frac{\Gamma(h\to\gamma\gamma)_{\rm BSM}}{\Gamma(h\to\gamma\gamma)_{\rm SM}}$. At one-loop level, the physical charged Higgs $H^\pm$ and fermion $E_1^\pm$ add extra contribution to the decay width $\Gamma(h\to\gamma\gamma)_{\rm BSM}$ as,

$$\Gamma(h\to\gamma\gamma)_{\rm BSM} = \frac{\alpha^2 M_h^3}{256\pi^3 v_1^2}\left|Q_{H^\pm}^2\frac{v_1 g_{hH^+H^-}}{2M_{H^\pm}^2}F_0(\tau_{H^\pm}) + Q_{E_1^\pm}^2 g_{hE_1^+E_1^-}F_{1/2}(\tau_{E_1^\pm}) + C_{\rm SM}\right|, \tag{36}$$

where $C_{\rm SM}$ is the SM particle's contributions,

$$C_{\rm SM} = \sum_f N_f^c Q_f^2 y_f F_{1/2}(\tau_f) + y_W F_1(\tau_W)$$

with $\tau_x = \frac{M_h^2}{M_x^2}$. Q stands for the electric charge of particles, and N_f^c denotes the color factor. The loop functions

$F_{(0,1/2,1)}(\tau)$ can be found in Ref. [36]. The coupling strengths are,

$$g_{hH^+H^-} = -(\cos\alpha\lambda_3 v_1) + \kappa_{\phi_1 s_2} \sin\alpha v_s, \qquad g_{hE_1^+E_1^-} = 0$$

at tree level.

E. Z' searches at LHC

The presence of Z' in the particle content which mixes with SM gauge boson Z will lead to the constraints on, $Z - Z'$ mixing angle, which should be less than 10^{-3}, so that well-measured Z decay width to various SM modes, does not modify much [15]. Drell-Yan dilepton (e, μ) resonance of Z' constraint from LHC [16–18] must also be considered. In this model the SM particle contents are neutral under the new gauge symmetry and they only couple to Z' through the GKM. The above collider bounds can be evaded by keeping a small GKM, so that the production cross section of dilepton pairs via Z' resonance at LHC lies below the current experimental limit.

F. Lepton flavor violation constraints

In the SM, lepton flavors (electron, muon, and tau) are conserved, meaning that charged leptons only interact with their corresponding neutrinos and do not change flavors. However, neutrino oscillations data predict the possibility of lepton flavor violation (LFV), where a neutrino of one flavor can transform into another. LFV processes can also occur through the exchange of new particles. In this model, the presence of dark sector scalars and fermions introduces new interactions that couple to all the SM-charged leptons, potentially leading to lepton flavor-violating processes, e.g., $\mu \to e\gamma$, $\tau \to \mu\gamma$, $\mu \to 3e$, etc. The magnetic momentum of SM-charged leptons is also affected by these couplings. The possible processes are shown in Fig. 1.

The $Y_{X_i,d_i,\nu_i} \sim 0.1$ with $M_{E_i} = \mathcal{O}(1)$ TeV lead to large LFV which is excluded by present data $\mathrm{BR}(\mu \to e\gamma) < 4.2 \times 10^{--13}$ [37], $\mathrm{BR}(\tau \to e\gamma) < 3.3 \times 10^{--8}$ and $\mathrm{BR}(\tau \to \mu\gamma) < 4.4 \times 10^{--8}$ [38]. However, by utilizing the first or second-generation Yukawa couplings ($i = 1$ or 2), with values below 10^{-3}, while keeping other couplings at the order of magnitude $\mathcal{O}(1)$, one can effectively circumvent the constraints imposed by LFV. We also find that large Yukawa couplings ($Y_{X_i,d_i,\nu_i} > 4\pi, i = 1, 2, 3$ with $M_{E_i} = \mathcal{O}(1)$ TeV) are required to explain the current muon anomalous magnetic moment $\delta a_\mu = (2.49 \pm 0.48) \times 10^{-9}$ [39–41]. Hence muon anomalous magnetic moment cannot be explained within the perturbative regime. Although the measurement of the muon $g-2$ shows a 5.1σ deviation [39,42] from the Standard Model prediction [43], there is tension in determining the hadronic vacuum polarization contribution due to discrepancies between lattice QCD calculations [44–55] and experimental data from $e^-e^+ \to \pi^-\pi^+$ processes [56]. If we consider the hadronic vacuum polarization contribution from the lattice QCD computation the deviation of $(g-2)_\mu$ from SM prediction significantly decreased. Therefore, we will not address the muon $g-2$ puzzle in this work.

It is also to be noted that contributions to the lepton electric dipole moment (EDM) can indeed arise through one or more loops depending on the CP-violation [57–59] term in the scalar potential. In this model, we do not have such a term in the scalar sector. The contributions from new fermions are significantly suppressed by the masses of the new fermions and scalars in the loop. Additionally, the suppression is further enhanced by the chosen small value of the new Yukawa couplings. We have considered real couplings throughout our analysis except in the table in Table III. Using the masses of the new scalars and fermions, $Y_{f\nu}$, Y_{fx} values given in Table III. We find that with $Y_{fd_2} = Y_{fd_3} = 10^{-3}$ the electric dipole moment for the μ and τ to be $\leq \mathcal{O}(10^{-25})$ e. cm, for both the BPs. For electron there is no EDM generated at one loop. The current limit on the EDM for e,μ and τ are $\mathcal{O}(10^{-30})$, $\mathcal{O}(10^{-19})$ and $\mathcal{O}(10^{-17})$ e. cm respectively [60–64]. Therefore these BPs are allowed from the present experimental constraints.

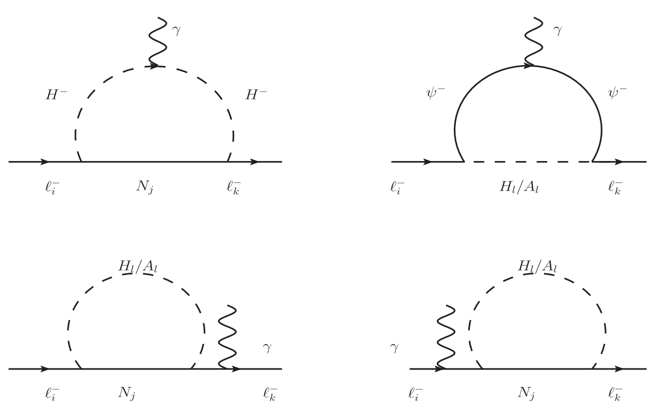

FIG. 1. Feynman diagrams contributing to $l_i^- \to l_k^- \gamma (i \neq k)$ process at one loop order.

G. Constraints from the neutrino low energy variables

The Yukawa Lagrangian given in Eq. (23) indicates that the mass of SM neutrinos cannot be obtained at the tree level. Instead, the neutrino mass arises through loop diagrams involving the Z_2 odd neutral fermions and scalars (see Fig. 2). We are able to generate the neutrino oscillation observables [65,66], shown in Table II. The phases α and δ

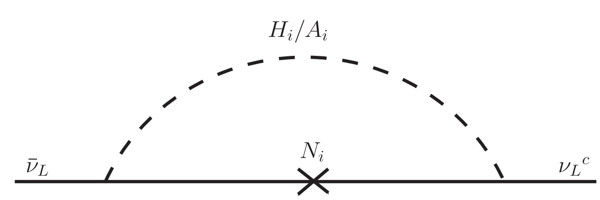

FIG. 2. Neutrino masses diagram at one loop when H_j/A_j ($j = d$, s) and N_i ($i = 1, 2, 3, 4$).

TABLE II. Neutrino oscillation data within 3σ range. The CP phase δ and Majorana phase α are still unconstrained from the experiment [65,66].

$\Delta m^2_{21}(10^{-5}\ \mathrm{eV}^2)$	$\Delta m^2_{31}(10^{-3}\ \mathrm{eV}^2)$	θ_{12}	θ_{13}	θ_{23}
6.82–8.04	2.430–2.593	31.27°–35.87°	8.25°–8.98°	39.7°–50.9°

are still unconstrained from the experiment. These experimental data restrict the parameters involved in generating neutrino mass and mixing angles. We discuss the detailed parameters in the numerical section.

H. Constraints from dark matter

The combined results from the Wilkinson Microwave Anisotropy Probe (WMAP) satellite, along with other cosmological measurements, have provided constraints on the DM relic density as $\Omega h^2 = 0.1198 \pm 0.0012$ [67]. Recent direct-detection experiments, such as Xenon-1T [68], LUX-ZEPLIN (LZ) [69], and PANDAX [70], have searched for the presence of weakly interacting massive particles (WIMPs) as potential DM candidates and put stringent bound on DM-nucleon scattering cross-secton. We consider a scalar DM scenario in this model and therefore we shall consider the constraints on the spin-independent (SI) cross section for direct detection in our analysis. In this model, the contribution to SI cross section comes from only the Higgs (light and heavy CP-even) mediated channel. For the DM mass of $\mathcal{O}(10\text{–}1000)$ GeV the stringent bound comes from recent XENON-1T [68] experiment with $\mathcal{O}(10^{-46}\text{–}10^{-45})\ \mathrm{cm}^2$. The null results from these experiments and data from collider experiments that include the invisible Higgs decay (into DM) and the Z boson decay width, put constraints on the couplings and mass of the DM.

In this work, we first use FeynRules [71] to build the model and then take the help of micrOMEGAs [72] to compute the relic density of the scalar DM. We also verified these using SARAH-4.14.3 [73,74] including Spheno-4.0.3 [75] mass spectrum in micrOMEGAs. We present a detailed discussion on DM in the next numerical analysis section.

IV. NUMERICAL ANALYSIS

In this section, we present our numerical results for the neutrino sector and DM phenomenology that will provide an insight on the characteristics of these elusive particles and their interaction properties.

A. Light neutrino masses and mixing angles

The nature of the neutrino mass term generated at one loop (see Fig. 2) from the Lagrangian (Eq. (23) is Majorana, and its magnitude is determined by the Yukawa couplings, namely Y_{fx}, $Y_{f\nu}$ and the masses of Z_2 odd charge neutral scalars and fermions. The detailed expression for neutrino mass matrix at one loop level is given by [19],

$$(\mathcal{M}_\nu)_{ij} = \sum_k \sum_l \frac{M^2_{H_l} M_k h^l_{ik} h^l_{jk} \ln\left(\frac{M^2_{H_l}}{M^2_k}\right)}{16\pi^2 (M^2_{H_l} - M^2_k)} - \sum_k \sum_l \frac{M^2_{A_l} M_k a^l_{ik} a^l_{jk} \ln\left(\frac{M^2_{A_l}}{M^2_k}\right)}{16\pi^2 (M^2_{A_l} - M^2_k)} \tag{37}$$

where h^l_{ik} and a^l_{ik} are coupling of Z_2 odd CP-even and odd scalar fields with BSM neutral fermions and neutrinos respectively, are given by,

$$h^l_{ik} = \frac{1}{\sqrt{2}}(\mathcal{U}_{N_{k2}} Z_{H_{l2}} Y_{fx_i} - \mathcal{U}_{N_{k4}} Z_{H_{l1}} Y_{f\nu_i}),$$
$$a^l_{ik} = \frac{1}{\sqrt{2}}(\mathcal{U}_{N_{k2}} Z_{A_{l2}} Y_{fx_i} - \mathcal{U}_{N_{k4}} Z_{A_{l1}} Y_{f\nu_i}).$$

The scalar mixing parameters Z_H and Z_A are given in Sec. II A, while the fermionic mixing matrix $\mathcal{U}_N$ is shown in Eq. (25). Note that to achieve a nonzero neutrino mass at the one-loop level, it is crucial to have a mass difference between the scalar (H_l) and pseudoscalar (A_l) particles. This mass difference is generated by the trilinear scalar term μ_S shown in Eq. (5). To get the neutrino mass eigenvalues, we have to diagonalize the above mass matrix using the well-established Pontecorvo–Maki–Nakagawa–Sakata (PMNS) matrix as $m_{\mathrm{diag}} = U^\dagger_{\mathrm{PMNS}} M_\nu U_{\mathrm{PMNS}}$. It is also essential to ensure that the choice of Yukawa couplings and other parameters involved in light neutrino masses are consistent with the current neutrino oscillation data. The neutrino masses depend on various parameters from the scalar as well as the fermionic sectors. A small change in one of the sectors can lead to altering the neutrino masses and mixing angles. We present two benchmark points in Table III, that give the correct neutrino mass squared differences and mixing angles.

In BP1, the mass difference between the CP-even and CP-odd sectors of the Z_2-odd scalar particle is extremely small [$\mathcal{O}$(MeV)], which helps us get the observed neutrino data for $\mathcal{O}(0.1 - 10^{-3})$ Yukawa couplings. We will see that such choices of nearly degenerate scalar masses leads to a considerable increase in coannihilation processes in the DM sector, ultimately resulting in a reduced relic density of DM. We also find that even with a significantly larger mass gap between the scalar particles, as shown in BP2, one can still generate all the correct neutrino mass differences and mixing angles, provided the relevant Yukawa couplings are chosen much smaller.

TABLE III. Two BPs satisfying the neutrino oscillation data. In BP1, mass difference between CP-even and CP-odd scalars are small hence Yukawa of $\mathcal{O}(10^{-4}–10^{-3})$ are required to satisfy neutrino observables, while for BP2, mass gap between CP-even and CP-odd scalars are larger therefore, smaller Yukawa coupling need to satisfy neutrino oscilation data.

	BP1	BP2
$M_N = \frac{1}{2} Y_{N_1} v_s$ (GeV)	500	500
M_L (GeV)	1000	1000
M_{H_1} (GeV)	460.0012	479
M_{H_2} (GeV)	400	400
M_{A_1} (GeV)	460	480
M_{A_2} (GeV)	400.0012	580
$\cos\beta$	0.710	0.910
$Y_{f\nu_i}$	2.87061×10^{-4}	9.5653×10^{-7}
	$(3.22832 - 0.457563i) \times 10^{-3}$	$(1.277 + 0.0884i) \times 10^{-5}$
	1.8424×10^{-3}	3.751×10^{-6}
Y_{fx_i}	3.366×10^{-4}	1.8174×10^{-5}
	$(3.0277 - 0.462412i) \times 10^{-3}$	$(-4.5597 + 0.919i) \times 10^{-6}$
	$(1.61062 - 0.0321793i) \times 10^{-3}$	$(-1.909 + 1.533i) \times 10^{-6}$
$\Delta m_{21}^2 (10^{-5}\ \mathrm{eV}^2)$	7.62246	7.4539
$\Delta m_{31}^2 (10^{-3}\ \mathrm{eV}^2)$	2.44989	2.5468
θ_{12}	33.4605°	33.4605°
θ_{13}	8.6192°	8.6192°
θ_{23}	42.1304°	42.1304°
α	80°	75°
δ	200°	200°

B. Dark matter analysis

In our analysis, we assume that H_1 is the lightest neutral component among the Z_2-odd particles which is a potential DM candidate and can give observed relic density of the Universe. Depending on the mixing angle β in the Z_2 odd scalar sector, the DM candidate H_1 can belong to the doublet, singlet or be a linear combination of both. The parameter space of the model determines the correct DM relic density, which depends on the annihilation, coannihilation, and decay processes. The condition for a decay or a scattering process to be in thermal equilibrium is $\frac{\Gamma}{H(T)} \geq 1$, where Γ is the rate of the relevant process. For a decay process, Γ is the decay width of the decaying particle for that process, while for the annihilation process $\Gamma = n_{\mathrm{eq}}\langle\sigma v\rangle$ [76] where n_{eq} stands for the equilibrium number density [77] and $H(T)$ is the Hubble parameter [76]. We now discuss the DM phenomenology for the freeze-out mechanism, considering all the constraints discussed earlier. The DM annihilation occurred in the early Universe when it was in thermal equilibrium with other particles. As the Universe's temperature drops below the DM mass, its production from the bath particles gets suppressed. The DM freezes out when the effective annihilation rate of DM becomes less than the expansion rate of the Universe, resulting in a density determined by the specific parameter ranges. In this model, the observed DM relic density can be obtained through annihilation processes shown in Figs. 3 and 4 which depend upon the Higgs portal couplings and the Yukawa couplings Y_{fd}, $Y_{f\nu}$ and Y_{fx}. We will study the scenarios, where the DM scalar belongs dominantly to the $SU(2)$ doublet and when it is dominantly an SM singlet. We will also consider the scenario where the DM has a reasonable doublet-singlet admixture. Finally, we study the role of the new gauge boson Z' in achieving the correct DM relic density.

In the pure doublet scenario ($\cos\beta = 1$), if we remove the new fermion and gauge particle effects, the DM behaves like the DM of an inert Higgs doublet model (IHDM) with the absence of the $\lambda_5(\Phi_1^\dagger\Phi_2)^2 + \mathrm{H.c.}$ term (see Ref. [78]), which means that $M_{H_1} = M_{A_1}$. This would mean that we never achieve observed relic density due to the large coannihilation contribution mediated by the SM Z boson. In order to control this large coannihilation, we need a mass splitting between the Z_2-odd CP-even and CP-odd scalar that suppresses the process. In this model such a splitting will be induced by the $(\sqrt{2}\mu_S S_2^2 S_1 - \mu_h \Phi_2^\dagger \Phi_1 S_2 + \mathrm{H.c.})$ terms in the scalar potential [Eq. (5)]. The larger the mass splitting, the more the coannihilation rate is suppressed. Thus, this mass splitting can be adjusted to achieve the desired coannihilation rate and match the observed DM relic density. In scenarios where the mass differences between the DM and the other dark sector particles are large, the coannihilation processes become inefficient for producing the correct DM relic density. In such cases, we rely on DM pair annihilation through the scalar mediators (h and H),

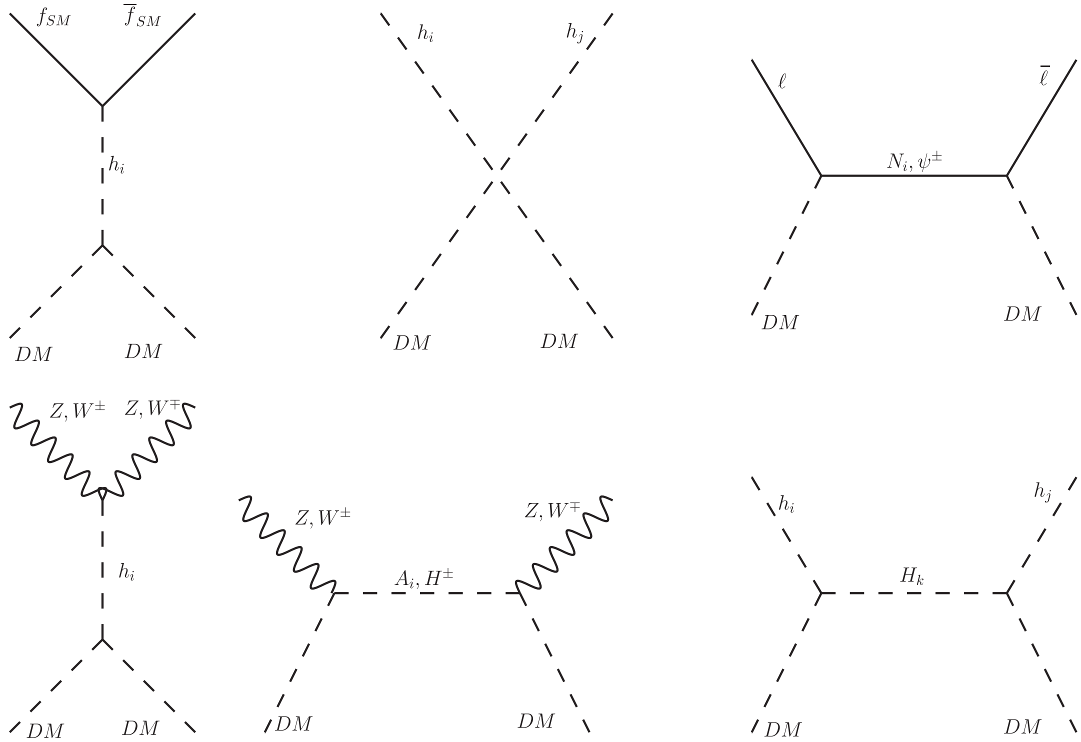

FIG. 3. The DM annihilation diagrams give the relic density. The vertical axis represents time.

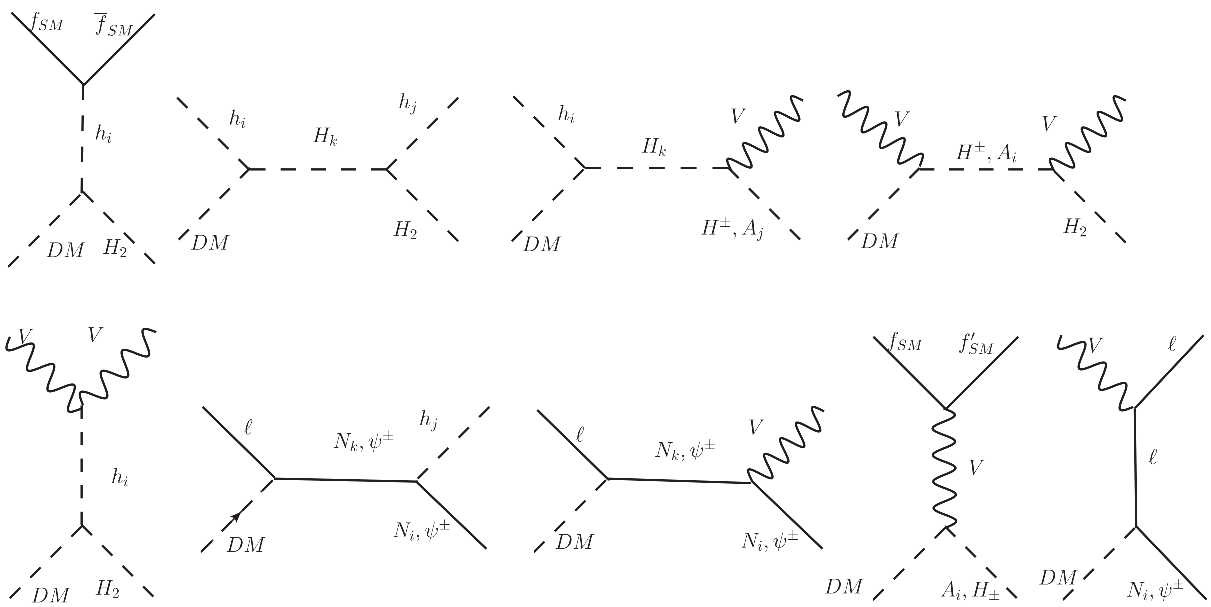

FIG. 4. The coannihilation and annihilation diagrams of the DM and the other Z_2-odd fermion fields. The vertical axis represents time.

interacting via scalar portal couplings $g_{hH_1H_1}$ and $g_{HH_1H_1}$, respectively. However, to satisfy relic density we would need very large Higgs coupling strength with the DM,

$$g_{hH_1H_1} \sim \cos^2\beta(\lambda_3+\lambda_4)v_1 - \frac{2\cos^2\beta\sin^2\beta(M_{H_2}^2 - M_{H_1}^2)}{v_1} - \cos\beta\sin\beta\kappa_4 v_s + \kappa_1 \sin^2\beta v_1.$$

In such a scenario, most of these points will be excluded by either the direct detection (DD) experiments or Higgs invisible decay width data that depend on the very same large couplings. Near, $M_{\rm DM} \approx \frac{M_h}{2}$, DM can resonantly annihilate to SM Higgs which then decays to SM particles. In the resonance region, a significantly smaller Higgs portal coupling will be sufficient to generate a large annihilation rate that leads to the correct DM relic density. As the

TABLE IV. Dominated (Co)annihilation processes. H_1 is mostly coming from CP-even component of Z_2-odd scalar doublet. The fermionic t, u-channel contributions almost zero due to small Yukawa couplings.

Sl. No.	Mixing $\cos\beta$	M_{DM} (GeV)	M_{H_2} (GeV)	M_{A_1} (GeV)	$M_{H^\pm}$ (GeV)	$Y^{1,3}_{fd,\nu}$	$Y^{1,3}_{fx}$	$\Omega_{\mathrm{DM}}h^2$	DD Cross (cm^3/s)	Contributions
D-type BP-1	0.9	45.0	86.9	54.71	130.0	10^{-4}	10^{-4}	0.1205	5.5×10^{-48}	$A_1A_1\to b\bar{b}$ 15% $H_1A_1\to q\bar{q}$ 54% $H_1A_1\to l\bar{l}$ 9% $H_1A_1\to \nu_l\bar{\nu}_l$ 21%
D-type BP-2	0.9	53.0	92.50	61.777	133.5	10^{-4}	10^{-4}	0.1199	5.4×10^{-48}	$A_1A_1\to b\bar{b}$ 18% $H_1A_1\to q\bar{q}$ 50% $H_1A_1\to l\bar{l}$ 9% $H_1A_1\to \nu_l\bar{\nu}_l$ 21% $H_1H_1\to WW^*$ 1%
D-type BP-3	0.9	72.5	128.14	84.206	152.5	10^{-4}	10^{-4}	0.1198	5.4×10^{-48}	$H_1H_1\to WW^*$ 80% $H_1H_1\to ZZ^*$ 5% $H_1A_1\to q\bar{q}$ 10% $H_1A_1\to \nu_l\bar{\nu}_l$ 5%

couplings are now suppressed, this would help evade the DD constraint and Higgs invisible decay bound.

Note that the coannihilation channels become crucial for determining the relic density of DM in the regions below and above $M_{\mathrm{DM}}\approx\frac{M_h}{2}$. The above-mentioned coannihilation channel is most dominant when the DM annihilates with the CP-odd scalar through the SM Z boson, particularly when their combined mass is near the Z resonance. We find that $M_{H_1}+M_{A_1}-M_Z\simeq 25$ GeV also results in dominant coannihilation. Table IV presents a couple of representative benchmark points where $M_{\mathrm{DM}}=45, 53$ GeV, that highlight the contribution of this coannihilation process in achieving the correct DM relic density. We have set the mixing angle $\cos\beta$ to 0.9 that leads to a scalar DM whose dominant composition comes from the Z_2-odd scalar doublet. Since the DM belongs to the $SU(2)_L$ scalar doublet, we avoid mass regions with $M_{H_1}+M_{A_1}<M_Z$ to prevent any alteration to the well-measured Z boson decay width and branching ratio to SM particles. It is worth pointing out that in the above mentioned benchmark points, with $M_{\mathrm{A}_1}=54.7$ GeV and 61.7 GeV, the two A_1 particles also annihilate via off-shell SM Higgs to $b\bar{b}$, effectively reducing the total number density of the Z_2 odd sector and contributing to the DM relic density.

Similar to the SM Z resonance, one can also exploit the resonant region due to the SM Higgs that leads to large rate for DM pair annihilation. We show two benchmark points near the Higgs resonance region in Table V with $M_{H_1}=58.82$ and 62.77 GeV. We choose smaller Higgs portal couplings ($g_{hH_1H_1}$) to get annihilation rate $\langle\sigma v\rangle\sim 2\times10^{-26}$ cm^3/s which gives exact relic density. These two points also comply with the Higgs invisible decay branching fraction constraint and bounds from DD experiments. Another important observation is that DM, being doubletlike, efficiently annihilates into gauge bosons such as WW^* and ZZ^* via the contact vertex and through the Z_2 odd sector particles in the t-channel. These DM annihilation channels significantly contribute to the DM relic density in these two representative points.

TABLE V. Dominated annihilation processes. H_1 is mostly coming from CP-even component of Z_2-odd scalar doublet. The fermionic t, u-channel contributions almost zero.

Sl. No.	Mixing $\cos\beta$	M_{DM} (GeV)	M_{H_2} (GeV)	M_{A_1} (GeV)	$M_{H^\pm}$ (GeV)	$Y^{1,3}_{fd,\nu}$	$Y^{1,3}_{fx}$	$\Omega_{\mathrm{DM}}h^2$	DD Cross (cm^3/s)	Contributions
D-type BP-4	0.9	58.82	144.44	77.419	138.82	10^{-4}	10^{-4}	0.1196	3.3×10^{-48}	$H_1H_1\to b\bar{b}$ 72% $H_1H_1\to q\bar{q}$ 5% $H_1H_1\to l\bar{l}$ 3% $H_1H_1\to WW^*$ 17% $H_1H_1\to ZZ^*$ 2%
D-type BP-5	0.9	62.77	148.41	80.995	142.77	10^{-4}	10^{-4}	0.1196	2.8×10^{-48}	$H_1H_1\to b\bar{b}$ 59% $H_1H_1\to q\bar{q}$ 4% $H_1H_1\to l\bar{l}$ 3% $H_1H_1\to WW^*$ 29% $H_1H_1\to ZZ^*$ 3%

In this model, similar to the inert doublet model [78], for doublet-type DM in region 72.5 GeV $< M_{\rm DM} <$ 400 GeV the processes $H_1 H_1 \to VV$ ($V = W$ and Z) become dominant and annihilate through standard gauge couplings. A large negative Higgs portal coupling is required to reduce the effective annihilation rate. However, direct detection data rules out such a large Higgs portal coupling, making it impossible to achieve the observed relic density in this region.

For doublet type DM with $M_{H_1} >$ 400 GeV, the relic density can be precisely obtained while satisfying various experimental constraints when the mass of the DM particle and other Z_2-odd particles is approximately equal, which leads to an enhancement of the coannihilation of DM with other dark sector particles. We show a few benchmark points to highlight our results in Table VI . Additionally, we have shown a plot of the DM relic density versus its mass in Fig. 5. Note that the long break in the relic density curve for the mass range 72.5 GeV $< M_{H_1} <$ 400 GeV corresponds to the case where the DM relic density cannot be satisfied due to the large annihilation rates of DM pair to SM gauge bosons, as discussed above. For $M_{H_1} >$ 400 GeV, the DM relic density is primarily satisfied due to the contributions coming from coannihilation processes. In this plot, the mixing angle is again fixed at $\cos\beta = 0.9$, and the mass of the other Z_2 odd particles are chosen to be close to the DM

TABLE VI. Dominated (Co)annihilation processes. H_1 is mostly coming from CP-even component of Z_2-odd scalar doublet. The fermionic t, u-channel contributions almost zero.

Sl. No.	Mixing $\cos\beta$	$M_{\rm DM}$ (GeV)	M_{H_2} (GeV)	M_{A_1} (GeV)	$M_{H^\pm}$ (GeV)	$Y^{1,3}_{fd,\nu}$	$Y^{1,3}_{fx}$	$\Omega_{\rm DM} h^2$	DD Cross (cm^3/s)	Contributions
D-type BP-6	0.9	420.0	420.01	420.002	420.1	10^{-4}	10^{-4}	0.1137	2.2×10^{-49}	$H^\pm H^\pm \to WW$ 18% $A_1 A_1 \to WW$ 9% $H^\pm A_1 \to \gamma W$ 9% $A_1 A_1 \to ZZ$ 8% $H^\pm H^\pm \to \gamma\gamma$ 8% $H^\pm H_1 \to \gamma W$ 7% $H^\pm H^\pm \to \gamma Z$ 6% $H_1 H_1 \to WW$ 6% $H_1 H_1 \to ZZ$ 6% $H_1 H_2 \to WW$ 4% $H_1 H_2 \to ZZ$ 3%
D-type BP-7	0.9	500.0	500.01	500.002	500.1	10^{-4}	10^{-4}	0.1161	4.0×10^{-49}	$H^\pm H^\pm \to WW$ 13% $A_1 A_1 \to WW$ 7% $H^\pm A_1 \to \gamma W$ 6% $A_1 A_1 \to ZZ$ 6% $H^\pm H^\pm \to \gamma\gamma$ 6% $H^\pm H_1 \to \gamma W$ 5% $H^\pm H^\pm \to \gamma Z$ 4% $H_1 H_1 \to WW$ 4% $H_1 H_1 \to ZZ$4% $H_1 H_2 \to WW$ 3% $H_1 H_2 \to ZZ$ 2% $H_1 H_1 \to l\bar{l}$ 1% $H^\pm H^\pm \to l\bar{l}$ 13%
D-type BP-8	0.9	700.0	701.61	700.303	701.605	10^{-4}	10^{-4}	0.1137	2.2×10^{-49}	$H^\pm H^\pm \to WW$ 3% $A_1 A_1 \to WW$ 14% $H^\pm A_1 \to \gamma W$ 2% $A_1 A_1 \to ZZ$ 5% $H^\pm H_1 \to \gamma W$ 2% $H_1 H_1 \to WW$ 9% $H_2 H_2 \to WW$ 7% $H_2 H_1 \to WW$ 13% $H_1 H_1 \to ZZ$ 5% $H_1 H_2 \to WW$ 4% $H_1 H_2 \to ZZ$ 3% $H^\pm H^\pm \to \gamma\gamma$ 1% $H^\pm H^\pm \to \gamma Z$ 1%

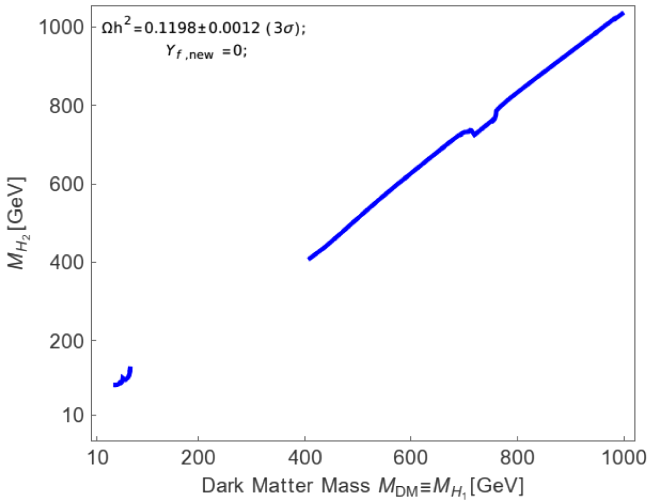

FIG. 5. We varied DM (doublet type, i.e., mixing angle $\cos\beta = 0.9$) mass and next-lightest Z_2 odd particle mass M_{H_2}. The DM $Y_f = 0$. Fermion masses $\sim$1 TeV, $M_{Z'} = 1$ TeV. The blue line gives relic density $\Omega h^2 = 0.1198 \pm 0.0012$ within 3σ, its also allowed by the direct detection experimental data. The other region is ruled out either from direct detection and or invisible decay width data or cannot satisfy the exact relic density.

mass. The heavy fermion masses are fixed as $(M_{N_1}, M_{N_2}, M_{N_3}, M_{N_4}, M_{\psi^\pm}) = (1.0, 1.0, 1.05, 1.5, 1.1)$ TeV in Fig. 5. A small dip appears around DM mass $M_{\rm DM} = 750$ GeV. It is due to the resonance channel $H_i H_j \to WW, ZZ, hh (i, j = 1, 2)$ via heavy CP-even Higgs H, with mass $M_H = 1500$ GeV. This indicates that the presence of an extra channel for DM annihilation requires decreasing the coannihilation contribution by increasing the mass difference between the DM and other dark sector particles.

So far, we have neglected any contributions from BSM fermions to the DM relic density by choosing relevant Yukawa couplings to be small. However, if we introduce these new fermionic interaction terms for doublet-type DM, we can achieve the correct DM relic density in the low DM mass region without relying on the SM Higgs resonance. This can be understood as follows: in the absence of new fermions, a significantly large Higgs portal coupling would be required to achieve the exact relic density. However, such a coupling is largely ruled out due to constraints from the invisible decay width of the Higgs boson and direct detection experiments. The terms $Y_{fd}\overline{\psi_L}\Phi_2 e_R + Y_{f\nu}\overline{\ell_L}\tilde{\Phi}_2 N_R +$ H.c. in the Lagrangian (23) induce annihilation processes, $H_1 H_1 \to \ell\bar{\ell}$ through these new fermions in the t-channel. These interactions can greatly impact the overall DM relic density. Here, l stands for SM leptons. Corresponding Feynman diagrams are shown in Fig. 4. We have shown a few corresponding benchmark points in the Table VII of this type. The term $Y_{fx}\overline{\psi_R}S_2\ell_L +$ H.c. in the Lagrangian (Eq. (23) can contribute to DM relic density for the doublet type of DM scenario via the mixing of CP-even scalar in the Z_2 odd sector through the above mentioned processes. We minimise the contribution of this term to the relic density by keeping Y_{fx} small.

One can see that the dominant contribution to the relic density in the low mass region mostly comes from the t channels annihilation processes with the BSM fermions in the propagator. For $M_{\rm DM} > 40$ GeV, the DM begins to annihilate into the SM gauge bosons via contact vertex. As these contributions become large, we need smaller Yukawa coupling to satisfy the DM relic density. This effect can be seen for the (D-type; BP-13) benchmark in the table.

We have plotted the DM mass against the new Yukawa couplings $Y_{fd} \equiv Y_{f\nu}$ in Fig. 6. The red line gives the correct relic density ($\Omega h^2 = 0.1198 \pm 0.0012$) within 3σ and is

TABLE VII. Dominated annihilation processes. H_1 is mostly coming from CP-even component of Z_2-odd scalar doublet. The fermionic t, u-channel contributions large.

Sl. No.	Mixing $\cos\beta$	$M_{\rm DM}$ (GeV)	M_{H_2} (GeV)	M_{A_1} (GeV)	$Y^{1,3}_{fd,\nu}$	$Y^{1,3}_{fx}$	$\Omega_{\rm DM}h^2$	DD Cross (cm^3/s)	Contributions
D-type BP-9	0.9	10.0	110.0	310	0.335	10^{-4}	0.1198	8.7×10^{-47}	$H_1H_1\to l\bar{l}$ 96% $H_1H_1\to\nu_l\bar{\nu}_l$ 4%
D-type BP-10	0.9	30.0	130.0	330	0.3256	10^{-4}	0.1198	1.2×10^{-47}	$H_1H_1\to l\bar{l}$ 96% $H_1H_1\to\nu_l\bar{\nu}_l$ 4%
D-type BP-11	0.9	50.0	150.0	350	0.324	10^{-4}	0.1198	5.5×10^{-48}	$H_1H_1\to l\bar{l}$ 96% $H_1H_1\to\nu_l\bar{\nu}_l$ 4%
D-type BP-12	0.9	70.0	170.0	370	0.288	10^{-4}	0.1198	2.5×10^{-48}	$H_1H_1\to l\bar{l}$ 68% $H_1H_1\to\nu_l\bar{\nu}_l$ 3% $H_1H_1\to WW^*$ 34% $H_1H_1\to ZZ^*$ 4%
D-type BP-13	0.9	74.0	173.8	373.8	0.1	10^{-4}	0.1138	1.2×10^{-48}	$H_1H_1\to l\bar{l}$ 16% $H_1H_1\to WW^*$ 77% $H_1H_1\to ZZ^*$ 6%

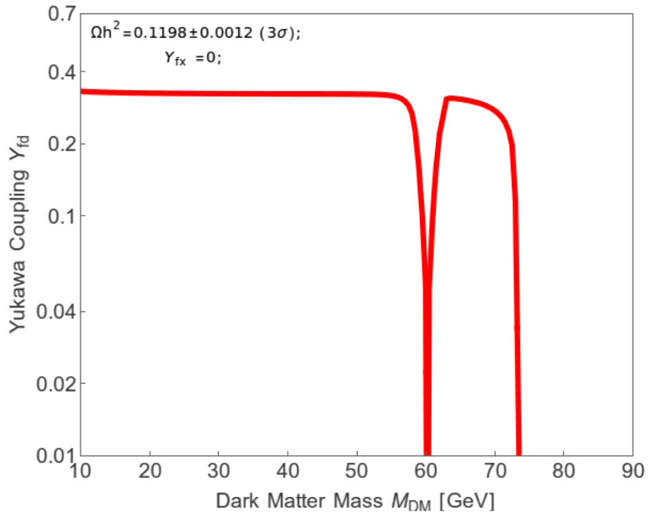

FIG. 6. We varied DM (doublet type, i.e., mixing angle 0.9 (red)mass and new Yukawa coupling $Y_{f_d} = Y_{f_\nu}$ with $Y_{f_x} = 0$. Fermion masses ∼1 TeV, $M_{Z'} = 1$ TeV. The red line gives relic density $\Omega h^2 = 0.1198 \pm 0.0012$ within 3σ, its also allowed by the invisible decay width and direct detection experimental data.

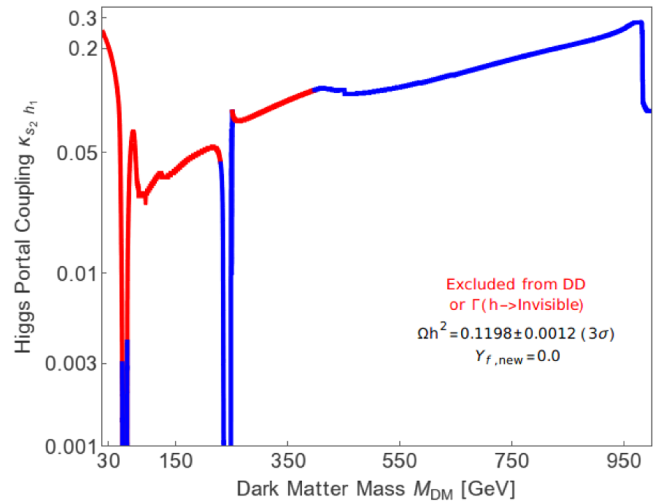

FIG. 7. We varied DM (mostly singlet type, i.e., mixing angle $\cos\beta = 0.05$) mass and Higgs portal coupling $\kappa_{\phi_1 s_2}$ with $Y_{f,x,d,\nu} = 0$, Fermion masses ∼1 TeV, $M_{Z'} = 1.5$ TeV, $M_H = 500$ GeV. The red-blue line gives relic density $\Omega h^2 = 0.1198 \pm 0.0012$ within 3σ. The red line excluded from Higgs Invisible decay width and/or the direct detection cross section.

also allowed by the invisible decay width constraints coming from the Higgs observation. The points on the curve are also consistent with the direct detection experimental data.

The singlet-type DM scenario is realized for a small mixing angle, $\cos\beta \sim 0$. For $M_{\rm DM} < 50$ GeV, the correct DM relic density can be again achieved through the Higgs portal coupling, where $\sin\beta \sim 1$:

$$g_{hH_1H_1} \sim \cos^2\beta(\lambda_3 + \lambda_4)v_1 - \frac{2\cos^2\beta\sin^2\beta(M_{H_2}^2 - M_{H_1}^2)}{v_1} - \cos\beta\sin\beta\kappa_4 v_s + \kappa_1\sin^2\beta v_1 \sim \kappa_1 v_1.$$

As before, there will be strong constraints on the strength of the Higgs portal coupling, coming from the invisible decay width of the SM Higgs boson as well as DD experiments. So we again rely on the contributions coming from the Higgs resonance region, i.e., at $M_{\rm DM} \approx M_h/2$, that leaves the possibility of a small Higgs portal coupling which can give $\langle\sigma v\rangle \sim 2\times 10^{-26}\ {\rm cm}^3/{\rm s}$. This can produce the correct relic density while remaining consistent with Higgs decay and DD constraints. The annihilation could also occur via the additional heavy CP-even scalar field H which couples with the DM through

$$g_{HH_1H_1} \sim \frac{4\mu_{\phi_{s2}}^2 + 2\kappa_{\phi_1 s_2}v_1^2 - 3M_{H_1}^2 - M_{A_2}^2}{2v_s}.$$

Due to this heavy Higgs, an additional resonance region can appear near $M_{H_1} = M_H/2$. It is important to note that achieving relic density is possible across a spectrum of DM masses, specifically within the $65 < M_{H_1} < 650$ GeV.[1] This outcome is contingent upon the specific value of the heavy Higgs mass (M_H). We illustrated the relic density (dominated by s- channel and cross-channels only, see Fig. 3) for the low as well as the high-DM mass region in $\kappa_{\phi_1 s_2} - M_{H_1}$ plane in Fig. 7. The solid red-blue band shows the relic density $\Omega h^2 = 0.1198 \pm 0.0012$ within 3σ. The red band is, however, excluded from the Higgs invisible decay or DD constraints as a large Higgs portal coupling is needed to get the correct DM relic density. In this plot two funnel like region appear near $M_{\rm DM} \approx \frac{M_h}{2}$ and $M_{\rm DM} \approx \frac{M_H}{2}$ with $M_H = 500$ GeV, which corresponds to the DM annihilation through the h and H resonance respectively. In these two funnel regions, the dominant channel is $H_1H_1 \to b\bar{b}$ for the low-DM mass range, whereas the high-mass region is dominated by $H_1H_1 \to \chi\chi$ channels. χ represents W, Z, t and h particles. The process $H_1H_1 \to HH$ also starts to contribute to the DM annihilation process near $M_{H_1} \approx M_H$. Hence a dip appears around $M_{\rm DM} = 500$ GeV. The vicinity of the DM mass at 950 GeV experiences a notable impact stemming from the coannihilation effect involving new heavy fermions, where the masses of these fermions are approximately 1 TeV. In this context, the DM annihilation through the t and u-channel BSM fermion exchange is negligible due to the choice of small new Yukawa couplings $Y_{fd,\nu,x}^{1,3} \approx 10^{-4}$. We present corresponding benchmark points for all the

[1]This region is ruled out in pure singlet scenario from direct detection experiments [79].

TABLE VIII. Dominated annihilation processes. H_1 is mostly coming from CP-even component of Z_2-odd scalar singlet. The fermionic t, u-channel contributions almost zero, coannihilation present depending on mass. The Fermion masses $\sim$1 TeV, $M_{Z'} = 1.5$ TeV.

Sl. No.	Mixing $\cos\beta$	$M_{\rm DM}$ (GeV)	M_{H_2} (GeV)	M_{A_1} (GeV)	$M_{H^\pm}$ (GeV)	$\kappa_{\phi_1 s_2}$	$Y^{1,3}_{fd,\nu,x}$	$\Omega_{\rm DM}h^2$	DD Cross (cm^3/s)	Contributions
S-type BP-1	0.05	56.0	356.0	356.0	656.0	0.00135	10^{-4}	0.1196	5.2×10^{-47}	$H_1H_1\to b\bar{b}$ 77% $H_1H_1\to WW^*$ 13% $H_1H_1\to c\bar{c}$ 6% $H_1H_1\to l\bar{l}$ 4% $H_1H_1\to ZZ^*$ 1%
S-type BP-2	0.05	62.9	360.9	360.9	660.9	0.001	10^{-4}	0.1203	3.1×10^{-47}	$H_1H_1\to b\bar{b}$ 71% $H_1H_1\to WW^*$ 19% $H_1H_1\to c\bar{c}$ 5% $H_1H_1\to l\bar{l}$ 3% $H_1H_1\to ZZ^*$ 2%
S-type BP-3	0.05	230.0	300.0	300.0	330.0	0.044	10^{-4}	0.1199	3.4×10^{-46}	$H_1H_1\to t\bar{t}$ 7% $H_1H_1\to WW$ 45% $H_1H_1\to ZZ$ 21% $H_1H_1\to hh$ 27%
S-type BP-4	0.05	400.0	470.0	470.0	500.0	0.115	10^{-4}	0.1211	6.1×10^{-46}	$H_1H_1\to t\bar{t}$ 6% $H_1H_1\to WW$ 46% $H_1H_1\to ZZ2$ 3% $H_1H_1\to hh$ 24%
S-type BP-5	0.05	950.0	1020.0	1020.0	1050.0	0.260	10^{-4}	0.1211	3.3×10^{-46}	$H_1H_1\to WW$ 32% $H_1H_1\to ZZ$ 16% $H_1H_1\to hh$ 16% $H_1H_1\to HH$ 6% $H_1H^\pm\to hW$ 4% $H_1H^\pm\to HW$ 3%
S-type BP-6	0.05	995.0	1060.0	1060.0	1095.0	10^{-4}	10^{-4}	0.1211	5.1×10^{-47}	$N_1E_1^\pm\to ZW^\pm$ 45% $N_1E_1^\pm\to hW^\pm$ 16% $N_1N_1\to Zh$ 9% $E_1E_1\to EE$ 13% $H_1H_1\to WW$ 2% $A_1A_1\to WW$ 1%

region discussed above and the contributions of different annihilation channels in Table VII.

Let us now examine how the BSM Yukawa couplings influence the computations of the relic density. The presence of the term $Y_{fx}\bar{\psi}_R S_2 \ell_L + \text{H.c.}$ in the Lagrangian [Eq. (23)] significantly enhance the annihilation rate of singlet-type DM as the DM can annihilate to SM leptons via t-channel diagram (see Fig. 4). For this scenario, we keep $Y^{1,3}_{fx} = \mathcal{O}(0.1)$ while ensuring the second component of $Y_{fx} \approx \mathcal{O}(10^{-4})$ to address potential issues related to LFV, particularly the constraints from the branching ratio of $\mu \to e\gamma$. Due to the presence of above mentioned Yukawa couplings ($Y^{1,3}_{fx}$) the observed relic can be achieved for a relatively low mass of DM ($\sim\mathcal{O}(10)$ GeV). These couplings compensate for the DM annihilation rate through the Higgs portal couplings by enabling new fermions-mediated channels. Therefore, for $M_{\rm DM} < \frac{M_h}{2}$, the correct DM relic density can be achieved while satisfying all relevant constraints, including the Higgs invisible decay width and direct detection constraints. We show a few benchmark points for the singlet-type DM scenario with the corresponding contributions of different annihilation channels for them in Table XIII. From the table, we observe that achieving the exact relic density is feasible solely through t-channel DM annihilation to the SM leptons mediated by these BSM fermions. For $M_{H_1} > 100$ GeV, the annihilation processes of H_1H_1 into WW, ZZ, and hh arising due to the exchange of dark sector scalars or through contact vertex can contribute to the relic density as depicted in the table.

We illustrate a permissible range of relic density within the $Y_{fx} - M_{H_1}$ parameter space, as depicted in Fig. 8. The plots have been produced for two distinct heavy Higgs mass values, namely $M_H = 1.5$ TeV and $M_H = 3$ TeV while the mass of the newly introduced fermions is 1 TeV.

TABLE IX. Higgs portal coupling is tiny. H_1 is mostly coming from CP-even component of Z_2-odd scalar doublet. The fermionic t, u-channel contributions large.

Sl. No.	Mixing $\cos\beta$	$M_{\rm DM}$ (GeV)	M_{H_2} (GeV)	M_{A_1} (GeV)	$M_{H^\pm}$ (GeV)	$Y^{1,3}_{fd,\nu}$	$Y^{1,3}_{fx}$	$\Omega_{\rm DM}h^2$	DD Cross (cm^3/s)	Contributions
S-type BP-7	0.05	10.0	110.0	109.81	130.0	10^{-4}	0.2696	0.1198	2.9×10^{-45}	$H_1H_1\to l\bar{l}$ 67% $H_1H_1\to \nu_l\bar{\nu}_l$ 32%
S-type BP-8	0.05	45.0	145.0	144.75	155.0	10^{-4}	0.2629	0.1198	1.4×10^{-46}	$H_1H_1\to l\bar{l}$ 65% $H_1H_1\to \nu_l\bar{\nu}_l$ 34%
S-type BP-9	0.05	100.0	200.0	199.70	180.0	10^{-4}	0.2631	0.1196	2.6×10^{-47}	$H_1H_1\to l\bar{l}$ 64% $H_1H_1\to \nu_l\bar{\nu}_l$ 33% $H_1H_1\to WW$ 2%
S-type BP-10	0.05	200.0	300.0	299.64	280.0	10^{-4}	0.2687	0.1198	5.7×10^{-49}	$H_1H_1\to l\bar{l}$ 68% $H_1H_1\to \nu_l\bar{\nu}_l$ 30% $H_1H_1\to WW$ 1%
S-type BP-11	0.05	600.0	700.0	699.56	680.0	10^{-4}	0.2924	0.1198	1.8×10^{-47}	$H_1H_1\to l\bar{l}$ 56% $H_1H_1\to \nu_l\bar{\nu}_l$ 30% $H_1H_1\to WW$ 7% $H_1H_1\to ZZ$ 4% $H_1H_1\to hh$ 4%

The funnel regions appear due to the CP-even scalar resonance in the annihilation channel, which would mean a dip in the contributions coming from the fermionic channels and therefore smaller values (dips in the figure) for the Yukawa couplings.

We also conduct a parameter scan involving variations in the Higgs portal coupling, new Yukawa coupling Y_{fx}, and DM mass. The results of this scan are presented in Fig. 9. The plot highlights regions in the coupling strengths of both fermionic and scalar interactions with the DM that contribute together to give the correct relic density. The definitive breakup of the regions where each are dominant has been discussed earlier. This plot is aimed at showing the wide range of the parameter choices that can achieve the correct relic density while satisfying all experimental constraints in the model. In our analysis, we have maintained certain parameters fixed, specifically setting $Y_{fd} = Y_{f\nu} \approx 0$, fermion masses at approximately 1 TeV, $M_H = 3$ TeV, and $M_{Z'} = 3$ TeV. The color points in the plot represent parameter combinations that satisfy the current relic density bound while adhering to all relevant theoretical and experimental constraints. Conversely, the empty region in the plot indicates parameter combinations that violate at least one of the imposed bounds. It could be due to the inconsistencies in DM relic density, detection experiments, Higgs decay width when the DM mass is less

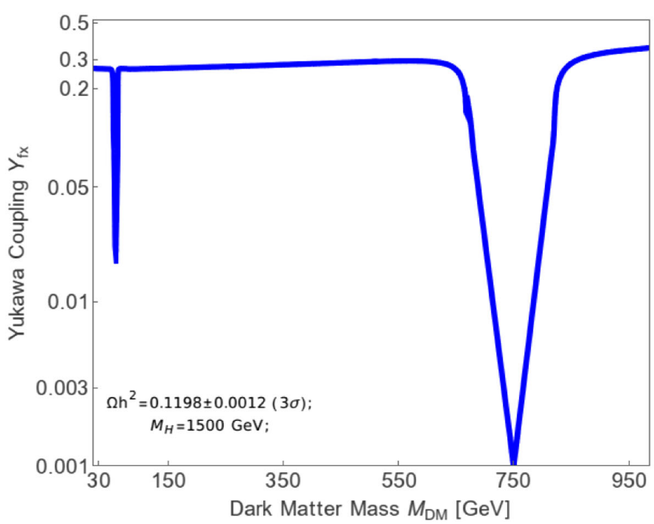

(a) (b)

FIG. 8. We varied DM (mostly singlet type, i.e., mixing angle $\cos\beta = 0.05$) mass and new Yukawa coupling Y_{f_x} with $Y_{f,d,\nu} = 0$, Fermion masses ∼1 TeV, $M_H = 1.5$ TeV and $M_H = 3$ TeV. The blue line gives relic density $\Omega h^2 = 0.1198 \pm 0.0012$ within 3σ.

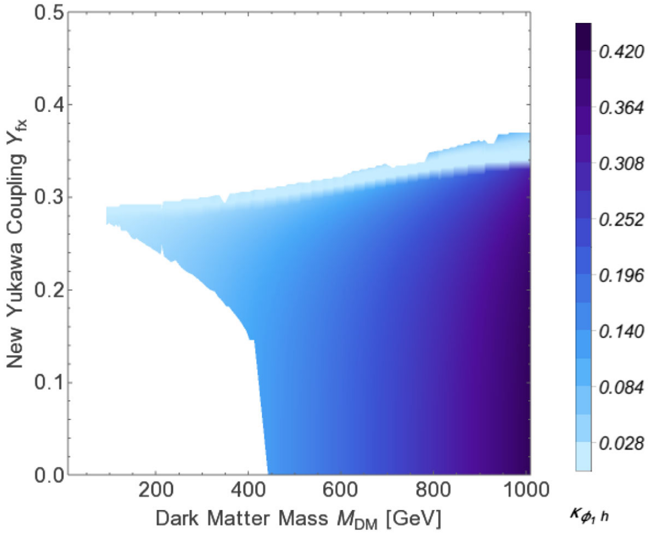

FIG. 9. We varied DM mass, Higgs portal coupling $\kappa_{\phi_1 s_2}$ and Yukawa couplings Y_{fx} here. All the blue shaded region provides relic density $\Omega h^2 = 0.1198 \pm 0.0012$ within 3σ, also satisfy all the theoretical and experimental constraints.

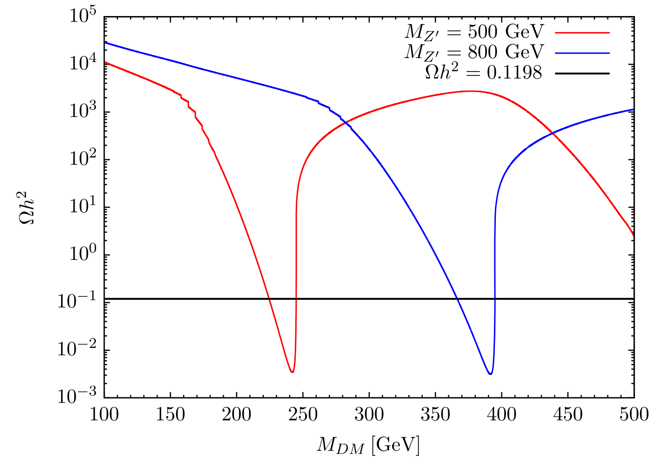

FIG. 11. We varied DM mass in the first plot for fixed $M_{Z'} =$ 0.5 and 0.8 TeV. The kinetic mixing $g'_x = 5 \times 10^{-3}$ and $M_A - M_{H_1} = 10$ GeV. All the Higgs portal couplings are zero in this plot.

than half of the Higgs mass or any other theoretical or experimental constraints considered in the analysis.

So far, we have discussed the role of scalar portal couplings and Yukawa couplings of the DM in achieving the observed DM relic density. When these couplings are very small, the DM annihilation is not efficient enough for obtaining the correct relic density. In such cases, we rely on the DM annihilation channels involving the new gauge boson Z' and the coupling g_x, as depicted in Fig. 10. The Z' directly couples to the DM particle, facilitating its production and annihilation processes in the early Universe and determining its relic density. Let us first consider the case where the DM mass ($M_{\rm DM}$) is less than $M_{Z'}$. In this scenario, DM can annihilate through the processes $H_1 H_1 \to Z'^* Z'^* (Z'^* \to f\bar{f})$ and/or $H_1 A_1 \to Z' \to f\bar{f}$. Here, A_1 represents the singlet-type pseudoscalar component, and f denotes the SM fermions. The coannihilation of M_{H_1} and M_{A_1} to SM fermions becomes significant near $M_{H_1} + M_{A_1} \sim M_{Z'}$ due to a resonance effect in the channel $H_1 A_1 \to Z' \to f\bar{f}$, that helps DM relic density to be satisfied. This effect is illustrated in Fig. 11 for $M_{Z'} = 500, 800$ GeV, where a nonzero value of gauge kinetic mixing $g'_x = 5 \times 10^{-3}$ is considered.

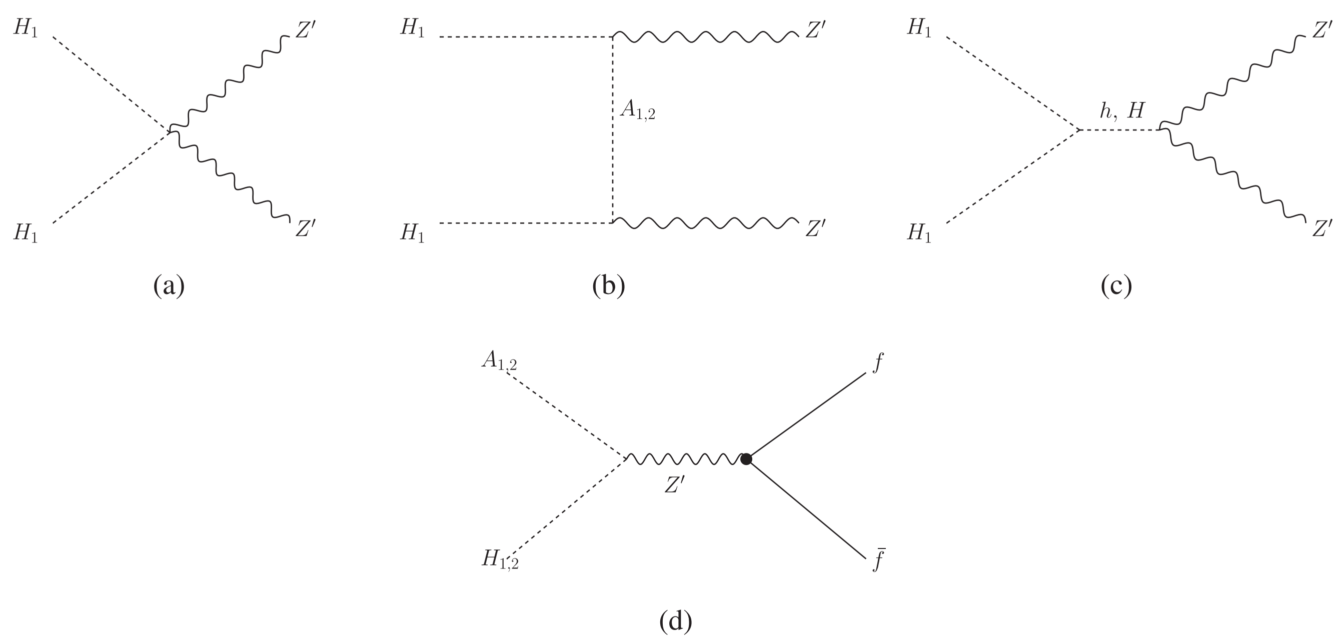

FIG. 10. Diagrams: DM annihilation into the new gauge bosons and fermions via gauge couplings. H_1 is the DM candidate, can be doublet or singlet type or admixture of these depending on the mixing angle β.

TABLE X. Higgs portal coupling is tiny. H_1 is mostly coming from CP-even component of Z_2-odd scalar singlet, $\cos\beta = 0.05$. The gauge kinetic mixing $g_{k,mix}$ is taken to be zero. The heavy scalar mass at $M_H = 3.0$ TeV.

Sl. No.	M_{DM} (GeV)	M_{H_2} (GeV)	M_{A_1} (GeV)	$M_{H^\pm}$ (GeV)	$M_{Z'}$ (GeV)	g_x	$g_{k,mix}$	$\Omega_{\mathrm{DM}}h^2$	DD Cross (cm^3/s)	Contributions
S-type BP-12	300.0	700.0	600.0	500.0	$0.50M_{\mathrm{DM}}$	0.1350	0.0	0.1198	$<10^{-60}$	$H_1H_1 \to Z'Z'$ 100%
S-type BP-13	300.0	700.0	600.0	500.0	$0.75M_{\mathrm{DM}}$	0.2103	0.0	0.1198	$<10^{-60}$	$H_1H_1 \to Z'Z'$ 100%
S-type BP-14	300.0	700.0	600.0	500.0	$0.90M_{\mathrm{DM}}$	0.2626	0.0	0.1198	$<10^{-60}$	$H_1H_1 \to Z'Z'$ 100%
S-type BP-15	800.0	1000.0	900.0	850.0	$0.50M_{\mathrm{DM}}$	0.2794	0.0	0.1198	$<10^{-60}$	$H_1H_1 \to Z'Z'$ 100%
S-type BP-16	800.0	1000.0	900.0	850.0	$0.75M_{\mathrm{DM}}$	0.3863	0.0	0.1198	$<10^{-60}$	$H_1H_1 \to Z'Z'$ 100%
S-type BP-17	800.0	1000.0	900.0	850.0	$0.90M_{\mathrm{DM}}$	0.4497	0.0	0.1198	$<10^{-60}$	$H_1H_1 \to Z'Z'$ 100%

When the mass of DM exceeds the $M_{Z'}$, the annihilation process of DM into $Z'Z'$ becomes possible kinematically, leading to an increase in the total annihilation cross section. Therefore, in this region we rely on the DM annihilation process $H_1H_1 \to Z'Z'$ to obtain the correct abundance of the DM in the Universe.

We estimate the contributions of the diagrams for the above process in the limit where only the gauge interactions are considered. Hence, only diagrams (a) and (b) of Fig. 10 contribute to the DM annihilation. We show some benchmark points for this scenario and the corresponding contributions of the annihilation channels in Table X.

We present the observed 3σ band of the DM relic density in the g_x-M_{DM} plane for three different values of n_f, in Fig. 12(a), where $n_f = M_{Z'}/M_{\mathrm{DM}}$. The plot can be interpreted in the following manner: for a given value of M_{DM}, increasing the Z' mass suppresses the DM annihilation cross section. A larger g_x value will then be needed to enhance the $\langle\sigma v\rangle$. Therefore the three curves representing the different ratios of the DM mass and Z' illustrate that heavier the DM mass, larger the gauge coupling g_x helps satisfy the correct relic density.

We now examine how the presence of scalar portal coupling of the DM changes the DM relic density computation in the region $M_{\mathrm{DM}} > M_{Z'}$. We consider the scenario with the heavy Higgs-mediated channels alongside the above mentioned channels. This also allows DM to annihilate into two Z' bosons via the heavy scalar H in an s-channel process. Figure 12(b) illustrates the influence of these extra channels on DM relic density, with $M_H = 1.5$ TeV. The dip in g_x around $M_{\mathrm{DM}} \approx 750$ GeV is a result of the heavy scalar resonance. Due to the presence of this additional annihilation channels for DM, a smaller g_x is required compared to Fig. 12(a) to achieve the correct DM relic density. We show some benchmark points of this type and corresponding contribution of the annihilation channels in Table XI.

V. COLLIDER SIGNATURE

We now briefly discuss some collider signatures of the model. Besides the usual signatures of a Z' at colliders

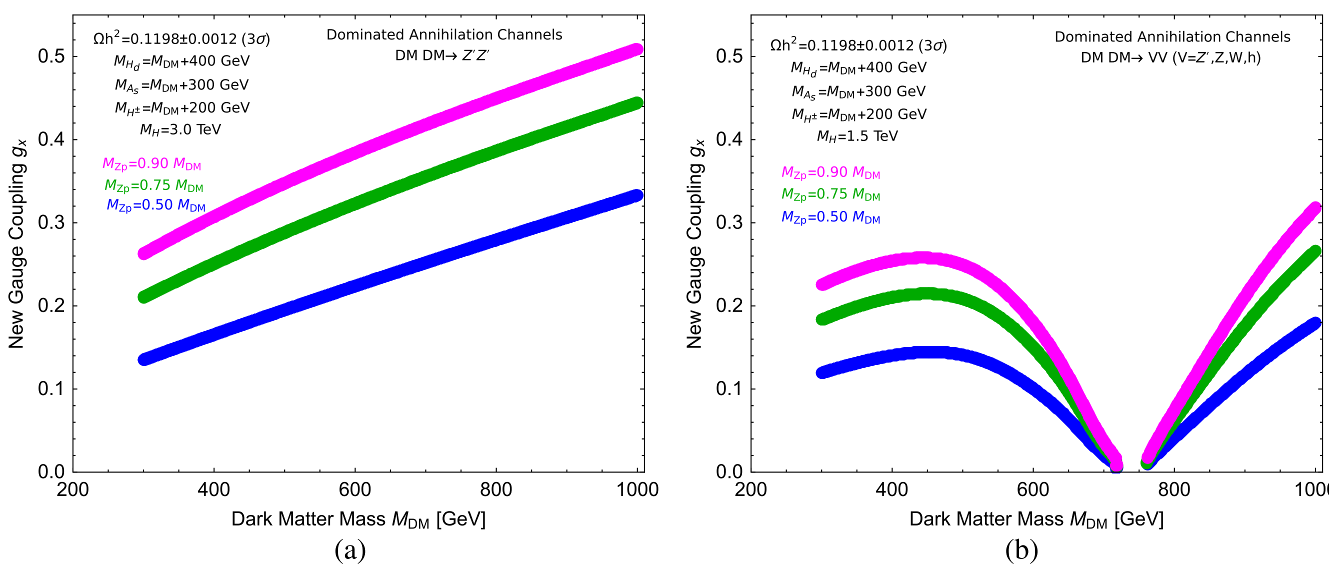

FIG. 12. We varied DM mass, gauge coupling g_x. The line gives relic density $\Omega h^2 = 0.1198 \pm 0.0012$ within 3σ, also satisfy all the theoretical and experimental constraints.

TABLE XI. Higgs portal coupling is tiny. H_1 is mostly scalar singlet-type DM. The gauge kinetic mixing $g_{k,mix}$ is zero with $M_H = 1.5$ TeV.

Sl. No.	M_{DM} (GeV)	M_{H_2} (GeV)	M_{A_1} (GeV)	$M_{H^\pm}$ (GeV)	$M_{Z'}$ (GeV)	g_x	$g_{k,mix}$	$\Omega_{\mathrm{DM}}h^2$	DD Cross (cm^3/s)	Contributions
S-type BP-18	300.0	700.0	600.0	500.0	$0.50M_{\mathrm{DM}}$	0.1194	0.0	0.1198	3.0×10^{-46}	$H_1H_1 \to Z'Z'$ 54% $H_1H_1 \to WW$ 21% $H_1H_1 \to hh$ 13% $H_1H_1 \to ZZ$ 9% $H_1H_1 \to t\bar{t}$ 4%
S-type BP-19	300.0	700.0	600.0	500.0	$0.75M_{\mathrm{DM}}$	0.1831	0.0	0.1198	2.8×10^{-46}	$H_1H_1 \to Z'Z'$ 51% $H_1H_1 \to WW$ 22% $H_1H_1 \to hh$ 13% $H_1H_1 \to ZZ$ 10% $H_1H_1 \to t\bar{t}$ 4%
S-type BP-20	300.0	700.0	600.0	500.0	$0.90M_{\mathrm{DM}}$	0.2250	0.0	0.1198	2.7×10^{-46}	$H_1H_1 \to Z'Z'$ 49% $H_1H_1 \to WW$ 23% $H_1H_1 \to hh$ 14% $H_1H_1 \to ZZ$ 10% $H_1H_1 \to t\bar{t}$ 4%
S-type BP-21	800.0	1000.0	900.0	800.0	$0.50M_{\mathrm{DM}}$	0.0414	0.0	0.1198	3.0×10^{-46}	$H_1H_1 \to Z'Z'$ 5% $H_1H_1 \to WW$ 46% $H_1H_1 \to hh$ 24% $H_1H_1 \to ZZ$ 20% $H_1H_1 \to t\bar{t}$ 4%
S-type BP-22	800.0	1000.0	900.0	800.0	$0.75M_{\mathrm{DM}}$	0.0621	0.0	0.1198	2.8×10^{-46}	$H_1H_1 \to Z'Z'$ 3% $H_1H_1 \to WW$ 46% $H_1H_1 \to hh$ 25% $H_1H_1 \to ZZ$ 20% $H_1H_1 \to t\bar{t}$ 4%
S-type BP-23	800.0	1000.0	900.0	800.0	$0.90M_{\mathrm{DM}}$	0.0746	0.0	0.1198	2.7×10^{-46}	$H_1H_1 \to Z'Z'$ 2% $H_1H_1 \to WW$ 47% $H_1H_1 \to hh$ 25% $H_1H_1 \to ZZ$ 20% $H_1H_1 \to t\bar{t}$ 4%

[80–84], the presence of a new fermionic sector which contains an $SU(2)$ doublet and SM singlet in addition to being odd under a discrete Z_2 symmetry, can lead to many interesting signatures of the model at collider experiments. Because of the Z_2 symmetry, these fermions when produced will always lead to signatures with missing energy in the final state. We highlight only a few of the signals here that give the monolepton and dilepton $+\not{E}_T$ with or without jets, multijet $+\not{E}_T$, etc. final states at the LHC. The production channels of these BSM scalars and fermions at LHC have been listed in Tables XII and XIII along with their possible decay channels.

We now discuss how the above final states are realized at LHC. The process $pp \to \psi^+\psi^-$, where $\psi^\pm$ represent the new charged fermions. These fermions can subsequently decay as $\psi^\pm \to W^\pm N_1$, with N_1 being the lightest BSM neutral fermion, followed by the decay $N_1 \to H_1\nu_i$ which is a completely invisible decay channel since H_1 is the DM. Thus the pair production of $\psi^+\psi^-$ will lead to W^+W^- and large missing energy in the final state. Therefore this

TABLE XII. The production channels of the dark sector scalars at LHC and their decay channels.

Processes	Mediators	Decay
$pp \to H^+H^-$	γ, Z, Z'	$H^\pm \to l^\pm N_1, \psi^\pm\nu, W^\pm H_1$
$pp \to H_1H^\pm$	$W^\pm$	$H^\pm \to l^\pm N_1, \psi^\pm\nu, W^\pm H_1$
$pp \to H_1A_1$	Z, Z'	$A_1 \to \nu N_1, ZH_1, Z'^*H_1, \psi^\pm l^\mp$
$pp \to H_2A_2$	Z'	$H_2 \to \psi^\pm l^\mp, \nu N_1,\ A_2 \to \psi^\pm l^\mp, \nu N_1, Z'^*H_2$

TABLE XIII. The production channels of the dark sector fermions at LHC and their decay channels.

Processes	Mediators	Decay
$pp \to \psi^+\psi^-$	γ, Z, Z'	$\psi^\pm \to l^\pm H_1, W^\pm N_1$
$pp \to \psi^\pm N_1$	$W^\pm$	$\psi^\pm \to l^\pm H_1, W^\pm N_1,\ N_1 \to \nu H_1$

channel with the above decay sequences gives rise to dilepton $+ \not{E}_T$, monolepton + dijet $+ \not{E}_T$ or 4 jets $+ \not{E}_T$ final states. The charged fermion $\psi^\pm$ can also decay via $\psi^\pm \to H_1 l$ for a given range of parameters. As H_1 is invisible, this decay sequence leads to the dilepton $+ \not{E}_T$ signature.

Consider the process $pp \to \psi^\pm N_1$ which is mediated by the W boson. Following the sequence of decays discussed above, the $\psi^\pm \to H_1 l; W^\pm N_1$, both modes lead to monolepton $+ \not{E}_T$ signature. Additionally, when the $\psi^\pm$ decays to $W^\pm N_1$, and W decays hadronically, we get the dijet $+ \not{E}_T$ final state as our signal.

The scalar production mode given by the process $pp \to H^+ H^-$, with the fermionic decay channels of $H^\pm$ as shown Table XII, also leads to the same final states as discussed above, with the only difference being the primary production channel of $H^+ H^-$ giving additional sources of missing energy in the cascades. Similarly, the process $pp \to H_1 H^\pm$ with $H^\pm \to W^\pm H_1$ can give rise to dijet + E_T and monolepton + E_T final state. It is worth noting that these channels can exhibit a significant production cross section at the LHC as these BSM particles have electroweak interactions. Moreover, as these particles are charged under the new gauge symmetry an additional diagram can contribute to the BSM scalar and fermion production at LHC via the Z' boson by introducing a nonzero gauge kinetic mixing. The Z' exchange in the s-channel can lead to a significant enhancement if the Z' is produced at resonance. In the process $pp \to A_{1,2} H_{1,2}$ the pseudoscalar $A_{1,2}$ can subsequently decay as $A_{1,2} \to Z/Z' H_{1,2}$, where Z/Z' denotes either the Standard Model Z boson or a new neutral gauge boson. The Z/Z' boson further decays in the visible channel as $Z/Z' \to ll$ or dijet, where l represents the SM charged lepton. Once again, this decay chain will result in the dilepton/dijet + E_T signature.

It is worth noting that the discussion on the collider signal has been limited to a very specific mass hierarchy in the particle spectrum in our current discussion (see Fig. 13). While there are indeed additional signals possible through various decay cascades of the produced particles in this model, a comprehensive analysis of these model particles and their properties is left for future work. These studies will aim to extract meaningful information about the properties of new particles, their interactions, and their role in the context of neutrino and DM including other constraints.

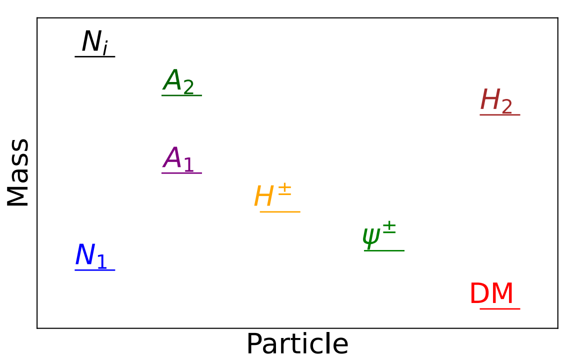

FIG. 13. The specific mass hierarchy for which collider signal has been discussed.

VI. CONCLUSIONS

In this study, we consider an additional $U(1)$ gauge symmetry along with the SM gauge symmetry. In addition to the standard model particles, our model incorporates vector-like doublet and singlet fermions, as well as two complex singlets and one doublet scalar field, which are charged under this new $U(1)$ gauge symmetry. All the SM particle contents are neutral under the new Abelian gauge symmetry. We explore the neutrino masses, mixing, and scalar dark matter in this model. We successfully achieve neutrino oscillation parameters and DM density within the expected range by selecting this field content. The neutrino mass and mixing angles are influenced significantly by the new Yukawa couplings and the mass differences between the Z_2-odd CP-even and CP-odd scalar particles. These parameters need to be extremely small to explain the observed neutrino properties. Interestingly, these same parameters are also directly linked to the DM abundance in the Universe. When the mass gap between these scalar particles is small, coannihilation processes become more prominent, while smaller Yukawa couplings result in reduced annihilation rates. We have examined these parameters extensively through careful analysis and discovered a significant region within the parameter space that yields interesting results.

To account for the observed relic density, we consider annihilation and coannihilation processes involving other particles in the model. Moreover, the new Yukawa terms enable the DM to annihilate into standard model particles through cross-channel, t-channel, and u-channel interactions. The interplay between these channels, characterized by constructive or destructive interference, effectively modifies the annihilation cross section. Consequently, our model obtains the correct relic density for the DM.

The Z' boson is crucial in obtaining the correct DM relic density as the DM is charged under the new gauge symmetry. Even in the absence of other portal coupling, we find that the new gauge coupling provides correct DM density obeying all the experimental and theoretical bounds.

ACKNOWLEDGMENTS

The authors would like to acknowledge the support from the Department of Atomic Energy (DAE), India, for the Regional Centre for Accelerator-based Particle Physics (RECAPP), Harish Chandra Research Institute.

APPENDIX

1. Stability constraints

The additional copositivity criteria [25] to have scalar potential bounded from below all the way.

$$\text{If } (\lambda_3+\lambda_4)<0 \ \&\ \lambda_{11}<0, \qquad \lambda_1\kappa_{s_1\phi_2}-(\lambda_3+\lambda_4)\lambda_{11}\geq\sqrt{(4\lambda_1\lambda_2-(\lambda_3+\lambda_4)^2)(4\lambda_1\lambda_{s2}-\lambda_{11}^2)},$$

$$\text{If } (\lambda_3+\lambda_4)<0 \ \&\ \lambda_{22}<0, \qquad \lambda_2\kappa_{s_2\phi_1}-(\lambda_3+\lambda_4)\lambda_{22}\geq\sqrt{(4\lambda_1\lambda_2-(\lambda_3+\lambda_4)^2)(4\lambda_2\lambda_{s2}-\lambda_{22}^2)},$$

$$\text{If } (\lambda_3+\lambda_4)<0 \ \&\ \kappa_{s_2\phi_1}<0, \qquad \lambda_1\lambda_{22}-(\lambda_3+\lambda_4)\kappa_{s_2\phi_1}\geq\sqrt{(4\lambda_1\lambda_2-(\lambda_3+\lambda_4)^2)(4\lambda_1\lambda_{s2}-\kappa_{s_2\phi_1}^2)},$$

$$\text{If } (\lambda_3+\lambda_4)<0 \ \&\ \kappa_{s_1\phi_2}<0, \qquad \lambda_2\lambda_{11}-(\lambda_3+\lambda_4)\kappa_{s_1\phi_2}\geq\sqrt{(4\lambda_1\lambda_2-(\lambda_3+\lambda_4)^2)(4\lambda_2\lambda_{s2}-\kappa_{s_1\phi_2}^2)},$$

$$\text{If } \lambda_{11}<0 \ \&\ \kappa_{s_2\phi_1}<0, \qquad \lambda_1\kappa_3-\lambda_{11}\kappa_{s_2\phi_1}\geq\sqrt{(4\lambda_1\lambda_{s2}-\lambda_{11}^2)(4\lambda_1\lambda_{s2}-\kappa_{s_2\phi_1}^2)},$$

$$\text{If } \kappa_{s_1\phi_2}<0 \ \&\ \lambda_{22}<0, \qquad \lambda_2\kappa_3-\lambda_{22}\kappa_{s_1\phi_2}\geq\sqrt{(4\lambda_2\lambda_{s2}-\lambda_{22}^2)(4\lambda_2\lambda_{s2}-\kappa_{s_1\phi_2}^2)},$$

$$\text{If } \lambda_{22}<0 \ \&\ \kappa_{s_1\phi_2}<0, \qquad \lambda_2\kappa_3-\lambda_{22}\kappa_{s_1\phi_2}\geq\sqrt{(\lambda_2\lambda_{s2}-\lambda_{22}^2)(\lambda_2\lambda_{s2}-\kappa_{s_1\phi_2}^2)},$$

$$\text{If } \lambda_{11}<0 \ \&\ \kappa_{s_1\phi_2}<0, \qquad (\lambda_3+\lambda_4)\lambda_{s2}-\lambda_{11}\kappa_{s_1\phi_2}\geq\sqrt{(4\lambda_1\lambda_{s2}-\lambda_{11}^2)(4\lambda_2\lambda_{s2}-\kappa_{s_1\phi_2}^2)},$$

$$\text{If } \lambda_{11}<0 \ \&\ \kappa_3<0, \qquad \lambda_{s2}\kappa_{s_2\phi_1}-\lambda_{11}\kappa_3\geq\sqrt{(4\lambda_1\lambda_{s2}-\lambda_{11}^2)(4\lambda_{s2}\lambda_{s2}-\kappa_3^2)},$$

$$\text{If } \kappa_{s_1\phi_2}<0 \ \&\ \kappa_3<0, \qquad \lambda_{22}\lambda_{s2}-\kappa_3\kappa_{s_1\phi_2}\geq\sqrt{(4\lambda_2\lambda_{s2}-\kappa_{s_1\phi_2}^2)(4\lambda_{s2}\lambda_{s2}-\kappa_3^2)}$$

$$\text{If } \kappa_3<0 \ \&\ \kappa_{s_1\phi_2}<0, \qquad \lambda_{22}\lambda_{s2}-\kappa_3\kappa_{s_1\phi_2}\geq\sqrt{(4\lambda_2\lambda_{s2}-\kappa_{s_1\phi_2}^2)(4\lambda_{s2}\lambda_{s2}-\kappa_3^2)},$$

$$\text{If } \lambda_{22}<0 \ \&\ \kappa_{s_2\phi_1}<0, \qquad (\lambda_3+\lambda_4)\lambda_{s2}-\lambda_{22}\kappa_{s_2\phi_1}\geq\sqrt{(4\lambda_2\lambda_{s2}-\lambda_{22}^2)(4\lambda_1\lambda_{s2}-\kappa_{s_2\phi_1}^2)},$$

$$\text{If } \lambda_{22}<0 \ \&\ \kappa_3<0, \qquad \lambda_{s2}\kappa_{s_1\phi_2}-\lambda_{22}\kappa_3\geq\sqrt{(4\lambda_2\lambda_{s2}-\lambda_{22}^2)(4\lambda_{s2}\lambda_{s2}-\kappa_3^2)},$$

$$\text{If } \kappa_3<0 \ \&\ \kappa_{s_2\phi_1}<0, \qquad \lambda_{11}\lambda_{s2}-\kappa_3\kappa_{s_2\phi_1}\geq\sqrt{(4\lambda_{s2}\lambda_{s2}-\kappa_3^2)(4\lambda_1\lambda_{s2}-\kappa_{s_2\phi_1}^2)},$$

$$\text{If } \lambda_{11}<0 \ \&\ \kappa_{s_1\phi_2}<0, \qquad (\lambda_3+\lambda_4)\lambda_{s2}-\lambda_{11}\kappa_{s_1\phi_2}\geq\sqrt{(4\lambda_1\lambda_{s2}-\lambda_{11}^2)(4\lambda_2\lambda_{s2}-\kappa_{s_1\phi_2}^2)},$$

2. Unitarity constraints

Various quartic couplings in nonphysical bases $\phi_{dr1}, \phi_{dr2}, \phi_{sr1}, \phi_{sr2}, \phi_{di1}(\equiv = G^0), \phi_{di2}, \phi_{si1}, \phi_{si2}, \phi_{d1}^{\pm}(\equiv = G^{\pm}), \phi_{d2}^{\pm}$,.

$$\{\phi_{dr1}\phi_{dr1}\phi_{dr1}\phi_{dr1}\}=6\lambda_1, \qquad \{\phi_{si1}\phi_{si1}\phi_{si2}\phi_{si2}\}=\kappa_3, \qquad \{\phi_{d1}^+\phi_{d1}^-\phi_{sr1}\phi_{sr1}\}=\lambda_{11},$$
$$\{\phi_{dr2}\phi_{dr2}\phi_{dr2}\phi_{dr2}\}=6\lambda_2, \qquad \{\phi_{dr1}\phi_{dr1}\phi_{di1}\phi_{di1}\}=2\lambda_1, \qquad \{\phi_{d1}^+\phi_{d1}^-\phi_{sr2}\phi_{sr2}\}=\kappa_{s_2\phi_1},$$
$$\{\phi_{sr1}\phi_{sr1}\phi_{sr1}\phi_{sr1}\}=6\lambda_{s1}, \qquad \{\phi_{dr1}\phi_{dr1}\phi_{di2}\phi_{di2}\}=\lambda_3+\lambda_4, \qquad \{H^+\phi_{d2}^-\phi_{dr1}\phi_{dr1}\}=\lambda_{22},$$
$$\{\phi_{sr2}\phi_{sr2}\phi_{sr2}\phi_{sr2}\}=6\lambda_{s2}, \qquad \{\phi_{dr1}\phi_{dr1}\phi_{si1}\phi_{si1}\}=\lambda_{11}, \qquad \{H^+\phi_{d2}^-\phi_{dr2}\phi_{dr2}\}=\lambda_3,$$
$$\{\phi_{di1}\phi_{di1}\phi_{di1}\phi_{di1}\}=6\lambda_1, \qquad \{\phi_{dr1}\phi_{dr1}\phi_{si2}\phi_{si2}\}=\kappa_{s_2\phi_1}, \qquad \{H^+\phi_{d2}^-\phi_{sr1}\phi_{sr1}\}=2\lambda_2,$$
$$\{\phi_{di2}\phi_{di2}\phi_{di2}\phi_{di2}\}=6\lambda_2, \qquad \{\phi_{dr2}\phi_{dr2}\phi_{di1}\phi_{di1}\}=\lambda_3+\lambda_4, \qquad \{H^+\phi_{d2}^-\phi_{sr2}\phi_{sr2}\}=\kappa_{s_1\phi_2},$$
$$\{\phi_{si1}\phi_{si1}\phi_{si1}\phi_{si1}\}=6\lambda_{s1}, \qquad \{\phi_{dr2}\phi_{dr2}\phi_{di2}\phi_{di2}\}=2\lambda_2, \qquad \{\phi_{d1}^+\phi_{d1}^-\phi_{di1}\phi_{di1}\}=2\lambda_1,$$
$$\{\phi_{si2}\phi_{si2}\phi_{si2}\phi_{si2}\}=6\lambda_{s2}, \qquad \{\phi_{dr2}\phi_{dr2}\phi_{si1}\phi_{si1}\}=\kappa_{s_1\phi_2}, \qquad \{\phi_{d1}^+\phi_{d1}^-\phi_{di2}\phi_{di2}\}=\lambda_3,$$
$$\{\phi_{dr1}\phi_{dr1}\phi_{dr2}\phi_{dr2}\}=\lambda_3+\lambda_4, \qquad \{\phi_{dr2}\phi_{dr2}\phi_{si2}\phi_{si2}\}=\lambda_{22}, \qquad \{\phi_{d1}^+\phi_{d1}^-\phi_{si1}\phi_{si1}\}=6\lambda_{11},$$

$$\begin{aligned}
&\{\phi_{dr1}\phi_{dr1}\phi_{sr1}\phi_{sr1}\} = \lambda_{11}, \qquad \{\phi_{sr1}\phi_{sr1}\phi_{di1}\phi_{di1}\} = \lambda_{11}, \qquad \{\phi^+_{d1}\phi^-_{d1}\phi_{si2}\phi_{si2}\} = \kappa_{s_2\phi_1},\\
&\{\phi_{dr1}\phi_{dr1}\phi_{sr2}\phi_{sr2}\} = \kappa_{s_2\phi_1}, \qquad \{\phi_{sr1}\phi_{sr1}\phi_{di2}\phi_{di2}\} = \kappa_{s_1\phi_2}, \qquad \{H^+\phi^-_{d2}\phi_{di1}\phi_{di1}\} = \lambda_3,\\
&\{\phi_{dr2}\phi_{dr2}\phi_{sr1}\phi_{sr1}\} = \kappa_{s_1\phi_2}, \qquad \{\phi_{sr1}\phi_{sr1}\phi_{si1}\phi_{si1}\} = 2\lambda_{\mathrm{s}1}, \qquad \{H^+\phi^-_{d2}\phi_{di2}\phi_{di2}\} = 2\lambda_2,\\
&\{\phi_{dr2}\phi_{dr2}\phi_{sr2}\phi_{sr2}\} = \lambda_{22}, \qquad \{\phi_{sr1}\phi_{sr1}\phi_{si2}\phi_{si2}\} = \kappa_3, \qquad \{H^+\phi^-_{d2}\phi_{si1}\phi_{si1}\} = \kappa_{s_1\phi_2},\\
&\{\phi_{sr1}\phi_{sr1}\phi_{sr2}\phi_{sr2}\} = \kappa_3, \qquad \{\phi_{sr2}\phi_{sr2}\phi_{di1}\phi_{di1}\} = \kappa_{s_2\phi_1}, \qquad \{H^+\phi^-_{d2}\phi_{si2}\phi_{si2}\} = \lambda_{22},\\
&\{\phi_{di1}\phi_{di1}\phi_{di2}\phi_{di2}\} = \lambda_3+\lambda_4, \qquad \{\phi_{sr2}\phi_{sr2}\phi_{di2}\phi_{di2}\} = \lambda_{22}, \qquad \{\phi^+_{d1}\phi^-_{d1}\phi^+_{d1}\phi^-_{d1}\} = 4\lambda_1,\\
&\{\phi_{di1}\phi_{di1}\phi_{si1}\phi_{si1}\} = \lambda_{11}, \qquad \{\phi_{sr2}\phi_{sr2}\phi_{si1}\phi_{si1}\} = \kappa_3, \qquad \{\phi^+_{d1}\phi^-_{d1}H^+\phi^-_{d2}\} = \lambda_3+\lambda_4,\\
&\{\phi_{di1}\phi_{di1}\phi_{si2}\phi_{si2}\} = \kappa_{s_2\phi_1}, \qquad \{\phi_{sr2}\phi_{sr2}\phi_{si2}\phi_{si2}\} = 2\lambda_{s2}, \qquad \{H^+\phi^-_{d2}H^+\phi^-_{d2}\} = 4\lambda_2,\\
&\{\phi_{di2}\phi_{di2}\phi_{si1}\phi_{si1}\} = \kappa_{s_1\phi_2}, \qquad \{\phi^+_{d1}\phi^-_{d1}\phi_{dr1}\phi_{dr1}\} = 2\lambda_1, \qquad \{H^+\phi^-_{d2}\phi_{si1}\phi_{si2}\} = 2\kappa_4,\\
&\{\phi_{di2}\phi_{di2}\phi_{si2}\phi_{si2}\} = \lambda_{22}, \qquad \{\phi^+_{d1}\phi^-_{d1}\phi_{dr2}\phi_{dr2}\} = \lambda_3,\\
&\{H^+\phi^-_{d2}\phi_{sr1}\phi_{sr2}\} = 2\kappa_4, \qquad \{H^+\phi^-_{d2}\phi_{sr1}\phi_{si2}\} = 2i\kappa_4,
\end{aligned}$$

The first 16×16 submatrix, corresponds to scattering processes whose initial and final states are one of $\phi^+_{d1}\phi_{di1}$, $\phi^+_{d1}\phi_{di2}$, $\phi^+_{d1}\phi_{si1}$, $\phi^+_{d1}\phi_{si2}$, $\phi^+_{d1}\phi_{dr1}$, $\phi^+_{d1}\phi_{dr2}$, $\phi^+_{d1}\phi_{sr1}$, $\phi^+_{d1}\phi_{sr2}$, $H^+\phi_{di1}$, $H^+\phi_{di2}$, $H^+\phi_{si1}$, $H^+\phi_{si2}$, $H^+\phi_{dr1}$, $H^+\phi_{dr2}$, $H^+\phi_{sr1}$, and $H^+\phi_{sr2}$ can be written as,

$$\mathcal{M}_1 = \begin{pmatrix}
2\lambda_1 & 0 & 0 & 0 & 0 & 0 & 0 & 0 & 0 & \frac{\lambda_4}{2} & 0 & 0 & 0 & -\frac{1}{2}(i\lambda_4) & 0 & 0\\
0 & \lambda_3 & 0 & 0 & 0 & 0 & 0 & 0 & \frac{\lambda_4}{2} & 0 & 0 & 0 & \frac{i\lambda_4}{2} & 0 & 0 & 0\\
0 & 0 & \lambda_{11} & 0 & 0 & 0 & 0 & 0 & 0 & 0 & 0 & 0 & 0 & 0 & 0 & 0\\
0 & 0 & 0 & \kappa_{s_2\phi_1} & 0 & 0 & 0 & 0 & 0 & 0 & 0 & \frac{1}{2}\kappa_4 & 0 & 0 & 0 & \frac{1}{2}i\kappa_4\\
0 & 0 & 0 & 0 & 2\lambda_1 & 0 & 0 & 0 & 0 & \frac{i\lambda_4}{2} & \frac{1}{2}\kappa_4 & 0 & 0 & \frac{\lambda_4}{2} & \frac{1}{2}i\kappa_4 & 0\\
0 & 0 & 0 & 0 & 0 & \lambda_3 & 0 & 0 & -\frac{1}{2}(i\lambda_4) & 0 & 0 & 0 & \frac{\lambda_4}{2} & 0 & 0 & 0\\
0 & 0 & 0 & 0 & 0 & 0 & \lambda_{11} & 0 & 0 & 0 & 0 & 0 & 0 & 0 & 0 & 0\\
0 & 0 & 0 & 0 & 0 & 0 & 0 & \kappa_{s_2\phi_1} & 0 & 0 & 0 & -\frac{1}{2}i\kappa_4 & 0 & 0 & 0 & \frac{1}{2}\kappa_4\\
0 & \frac{\lambda_4}{2} & 0 & 0 & 0 & \frac{i\lambda_4}{2} & 0 & 0 & \lambda_3 & 0 & -\frac{1}{2}i\kappa_4 & 0 & 0 & 0 & \frac{1}{2}\kappa_4 & 0\\
\frac{\lambda_4}{2} & 0 & 0 & 0 & -\frac{1}{2}(i\lambda_4) & 0 & 0 & 0 & 0 & 2\lambda_2 & 0 & 0 & 0 & 0 & 0 & 0\\
0 & 0 & 0 & \frac{1}{2}\kappa_4 & 0 & 0 & 0 & -\frac{1}{2}i\kappa_4 & 0 & 0 & \kappa_{s_1\phi_2} & 0 & 0 & 0 & 0 & 0\\
0 & 0 & \frac{1}{2}\kappa_4 & 0 & 0 & 0 & -\frac{1}{2}i\kappa_4 & 0 & 0 & 0 & 0 & \lambda_{22} & 0 & 0 & 0 & 0\\
0 & -\frac{1}{2}(i\lambda_4) & 0 & 0 & 0 & \frac{\lambda_4}{2} & 0 & 0 & 0 & 0 & 0 & 0 & \lambda_3 & 0 & 0 & 0\\
\frac{i\lambda_4}{2} & 0 & 0 & 0 & \frac{\lambda_4}{2} & 0 & 0 & 0 & 0 & 0 & 0 & 0 & 0 & 2\lambda_2 & 0 & 0\\
0 & 0 & 0 & \frac{1}{2}i\kappa_4 & 0 & 0 & 0 & \frac{1}{2}\kappa_4 & 0 & 0 & 0 & 0 & 0 & 0 & \kappa_{s_1\phi_2} & 0\\
0 & 0 & \frac{1}{2}i\kappa_4 & 0 & 0 & 0 & \frac{1}{2}\kappa_4 & 0 & 0 & 0 & 0 & 0 & 0 & 0 & 0 & \lambda_{22}
\end{pmatrix}, \tag{A1}$$

with eigenvalues: $\kappa_{s_2\phi_1}$, $\kappa_{s_1\phi_2}$, $2\lambda_1$, λ_{11}, λ_{22}, $2\lambda_2$, λ_3, $\lambda_3\pm\lambda_4$, $\lambda_1+\lambda_2\pm\sqrt{\lambda_1^2-2\lambda_2\lambda_1+\lambda_2^2+\lambda_4^2+4\kappa_4^2}$.

The second 14×14 submatrix, corresponds to scattering processes whose initial and final states are one of $\phi^+_{d1}\phi^-_{d2}$, $\phi^-_{d1}\phi^+_{d2}$, $\phi_{di1}\phi_{di2}$, $\phi_{di1}\phi_{si1}$, $\phi_{di1}\phi_{si2}$, $\phi_{di2}\phi_{si1}$, $\phi_{di2}\phi_{si2}$, $\phi_{si1}\phi_{si2}$, $\phi_{dr1}\phi_{dr2}$, $\phi_{dr1}\phi_{sr1}$, $\phi_{dr1}\phi_{sr2}$, $\phi_{dr2}\phi_{sr1}$, $\phi_{dr2}\phi_{sr2}$, and $\phi_{sr1}\phi_{sr2}$ is given by,

$$
\mathcal{M}_2 = \begin{pmatrix}
\lambda_3+\lambda_4 & 0 & \frac{\lambda_4}{2} & 0 & 0 & 0 & 0 & \frac{1}{2}\kappa_4 & \frac{\lambda_4}{2} & 0 & 0 & 0 & 0 & \frac{1}{2}\kappa_4 \\
0 & \lambda_3+\lambda_4 & \frac{\lambda_4}{2} & 0 & 0 & 0 & 0 & \frac{1}{2}\kappa_4 & \frac{\lambda_4}{2} & 0 & 0 & 0 & 0 & \frac{1}{2}\kappa_4 \\
\frac{\lambda_4}{2} & \frac{\lambda_4}{2} & \lambda_3+\lambda_4 & 0 & 0 & 0 & 0 & \frac{1}{2}\kappa_4 & 0 & 0 & 0 & 0 & 0 & \frac{1}{2}\kappa_4 \\
0 & 0 & 0 & \lambda_{11} & 0 & 0 & \frac{1}{2}\kappa_4 & 0 & 0 & 0 & 0 & 0 & -\frac{1}{2}\kappa_4 & 0 \\
0 & 0 & 0 & 0 & \kappa_{s_2\phi_1} & \frac{1}{2}\kappa_4 & 0 & 0 & 0 & 0 & 0 & \frac{1}{2}\kappa_4 & 0 & 0 \\
0 & 0 & 0 & 0 & \frac{1}{2}\kappa_4 & \kappa_{s_1\phi_2} & 0 & 0 & 0 & 0 & \frac{1}{2}\kappa_4 & 0 & 0 & 0 \\
0 & 0 & 0 & \frac{1}{2}\kappa_4 & 0 & 0 & \lambda_{22} & 0 & 0 & -\frac{1}{2}\kappa_4 & 0 & 0 & 0 & 0 \\
\frac{1}{2}\kappa_4 & \frac{1}{2}\kappa_4 & \frac{1}{2}\kappa_4 & 0 & 0 & 0 & 0 & \kappa_3 & \frac{1}{2}\kappa_4 & 0 & 0 & 0 & 0 & 0 \\
\frac{\lambda_4}{2} & \frac{\lambda_4}{2} & 0 & 0 & 0 & 0 & 0 & \frac{1}{2}\kappa_4 & \lambda_3+\lambda_4 & 0 & 0 & 0 & 0 & 0 \\
0 & 0 & 0 & 0 & 0 & 0 & -\frac{1}{2}\kappa_4 & 0 & 0 & \lambda_{11} & 0 & 0 & \frac{1}{2}\kappa_4 & 0 \\
0 & 0 & 0 & 0 & 0 & \frac{1}{2}\kappa_4 & 0 & 0 & 0 & 0 & \kappa_{s_2\phi_1} & \frac{1}{2}\kappa_4 & 0 & 0 \\
0 & 0 & 0 & 0 & \frac{1}{2}\kappa_4 & 0 & 0 & 0 & 0 & 0 & \frac{1}{2}\kappa_4 & \kappa_{s_1\phi_2} & 0 & 0 \\
0 & 0 & 0 & -\frac{1}{2}\kappa_4 & 0 & 0 & 0 & 0 & 0 & \frac{1}{2}\kappa_4 & 0 & 0 & \lambda_{22} & 0 \\
\frac{1}{2}\kappa_4 & \frac{1}{2}\kappa_4 & \frac{1}{2}\kappa_4 & 0 & 0 & 0 & 0 & 0 & \frac{1}{2}\kappa_4 & 0 & 0 & 0 & 0 & \kappa_3
\end{pmatrix}, \tag{A2}
$$

having eigenvalues: $\kappa_{s_2\phi_1}$, $\kappa_{s_1\phi_2}$, κ_3, λ_3, $\lambda_3+\lambda_4$, $\lambda_3+2\lambda_4$, λ_{11}, λ_{22},$\frac{1}{2}(\lambda_{11}+\lambda_{22}\pm\sqrt{(\lambda_{11}-\lambda_{22})^2+4\kappa_4^2})$, $\frac{1}{2}(\kappa_{s_2\phi_1}+\kappa_{s_1\phi_2}\pm\sqrt{(\kappa_{s_2\phi_1}-\kappa_{s_1\phi_2})^2+4\kappa_4^2})$,$\frac{1}{2}(\lambda_3+2\lambda_4+\kappa_{s_1s_2}+\sqrt{8\kappa_4^2+(\lambda_3+2\lambda_4-\kappa_{s_1s_2})^2})$.

The third and most-stringent 10×10 submatrix $\mathcal{M}_3$, corresponds to scattering fields $\phi_{d1}^-\phi_{d1}^+$, $\phi_{d2}^-H^+$, $\frac{\phi_{di1}\phi_{di1}}{\sqrt{2}}$, $\frac{\phi_{di2}\phi_{di2}}{\sqrt{2}}$, $\frac{\phi_{si1}\phi_{si1}}{\sqrt{2}}$, $\frac{\phi_{si2}\phi_{si2}}{\sqrt{2}}$, $\frac{\phi_{dr1}\phi_{dr1}}{\sqrt{2}}$, $\frac{\phi_{dr2}\phi_{dr2}}{\sqrt{2}}$, $\frac{\phi_{sr1}\phi_{sr1}}{\sqrt{2}}$ and $\frac{\phi_{sr2}\phi_{sr2}}{\sqrt{2}}$. The factor $\frac{1}{\sqrt{2}}$ has appeared due to the statistics of identical particles. $\mathcal{M}_3$ is,

$$
\mathcal{M}_3 = \begin{pmatrix}
4\lambda_1 & \lambda_3+\lambda_4 & \sqrt{2}\lambda_1 & \frac{\lambda_3}{\sqrt{2}} & \frac{\lambda_{11}}{\sqrt{2}} & \frac{\kappa_{s_2\phi_1}}{\sqrt{2}} & \sqrt{2}\lambda_1 & \frac{\lambda_3}{\sqrt{2}} & \frac{\lambda_{11}}{\sqrt{2}} & \frac{\kappa_{s_2\phi_1}}{\sqrt{2}} \\
\lambda_3+\lambda_4 & 4\lambda_2 & \frac{\lambda_3}{\sqrt{2}} & \sqrt{2}\lambda_2 & \frac{\kappa_{s_1\phi_2}}{\sqrt{2}} & \frac{\lambda_{22}}{\sqrt{2}} & \frac{\lambda_3}{\sqrt{2}} & \sqrt{2}\lambda_2 & \frac{\kappa_{s_1\phi_2}}{\sqrt{2}} & \frac{\lambda_{22}}{\sqrt{2}} \\
\sqrt{2}\lambda_1 & \frac{\lambda_3}{\sqrt{2}} & 3\lambda_1 & \frac{1}{2}(\lambda_3+\lambda_4) & \frac{\lambda_{11}}{2} & \frac{1}{2}\kappa_{s_2\phi_1} & \lambda_1 & \frac{1}{2}(\lambda_3+\lambda_4) & \frac{\lambda_{11}}{2} & \frac{1}{2}\kappa_{s_2\phi_1} \\
\frac{\lambda_3}{\sqrt{2}} & \sqrt{2}\lambda_2 & \frac{1}{2}(\lambda_3+\lambda_4) & 3\lambda_2 & \frac{1}{2}\kappa_{s_1\phi_2} & \frac{\lambda_{22}}{2} & \frac{1}{2}(\lambda_3+\lambda_4) & \lambda_2 & \frac{1}{2}\kappa_{s_1\phi_2} & \frac{\lambda_{22}}{2} \\
\frac{\lambda_{11}}{\sqrt{2}} & \frac{\kappa_{s_1\phi_2}}{\sqrt{2}} & \frac{\lambda_{11}}{2} & \frac{1}{2}\kappa_{s_1\phi_2} & 3\lambda_{s1} & \frac{1}{2}\kappa_3 & \frac{\lambda_{11}}{2} & \frac{1}{2}\kappa_{s_1\phi_2} & \lambda_{s1} & \frac{1}{2}\kappa_3 \\
\frac{\kappa_{s_2\phi_1}}{\sqrt{2}} & \frac{\lambda_{22}}{\sqrt{2}} & \frac{1}{2}\kappa_{s_2\phi_1} & \frac{\lambda_{22}}{2} & \frac{1}{2}\kappa_3 & 3\lambda_{s2} & \frac{1}{2}\kappa_{s_2\phi_1} & \frac{\lambda_{22}}{2} & \frac{1}{2}\kappa_3 & \lambda_{s2} \\
\sqrt{2}\lambda_1 & \frac{\lambda_3}{\sqrt{2}} & \lambda_1 & \frac{1}{2}(\lambda_3+\lambda_4) & \frac{\lambda_{11}}{2} & \frac{1}{2}\kappa_{s_2\phi_1} & 3\lambda_1 & \frac{1}{2}(\lambda_3+\lambda_4) & \frac{\lambda_{11}}{2} & \frac{1}{2}\kappa_{s_2\phi_1} \\
\frac{\lambda_3}{\sqrt{2}} & \sqrt{2}\lambda_2 & \frac{1}{2}(\lambda_3+\lambda_4) & \lambda_2 & \frac{1}{2}\kappa_{s_1\phi_2} & \frac{\lambda_{22}}{2} & \frac{1}{2}(\lambda_3+\lambda_4) & 3\lambda_2 & \frac{1}{2}\kappa_{s_1\phi_2} & \frac{\lambda_{22}}{2} \\
\frac{\lambda_{11}}{\sqrt{2}} & \frac{\kappa_{s_1\phi_2}}{\sqrt{2}} & \frac{\lambda_{11}}{2} & \frac{1}{2}\kappa_{s_1\phi_2} & \lambda_{s1} & \frac{1}{2}\kappa_3 & \frac{\lambda_{11}}{2} & \frac{1}{2}\kappa_{s_1\phi_2} & 3\lambda_{s1} & \frac{1}{2}\kappa_3 \\
\frac{\kappa_{s_2\phi_1}}{\sqrt{2}} & \frac{\lambda_{22}}{\sqrt{2}} & \frac{1}{2}\kappa_{s_2\phi_1} & \frac{\lambda_{22}}{2} & \frac{1}{2}\kappa_3 & \lambda_{s2} & \frac{1}{2}\kappa_{s_2\phi_1} & \frac{\lambda_{22}}{2} & \frac{1}{2}\kappa_3 & 3\lambda_{s2}
\end{pmatrix}, \tag{A3}
$$

The eigenvalues cannot be calculated analytically. We get the analytical values for the choice of $\lambda_{11}=\lambda_{22}=\kappa_{s_2\phi_1}=\kappa_{s_1\phi_2}=0$. The eigenvalues are now: $2\lambda_1$, $2\lambda_2$, $2\lambda_{s1}$, $2\lambda_{s2}$, $\lambda_1+\lambda_2\pm\sqrt{(\lambda_1-\lambda_2)^2+\lambda_4^2}$, $3\lambda_1+3\lambda_2\pm\sqrt{9(\lambda_1-\lambda_2)^2+(2\lambda_3+\lambda_4)^2}$, and $2\lambda_{s1}+2\lambda_{s2}\pm\sqrt{\kappa_{s_1s_2}^2+4(\lambda_{s1}-\lambda_{s2})^2}$.

[1] G. Aad *et al.* (ATLAS Collaboration), Observation of a new particle in the search for the Standard Model Higgs boson with the ATLAS detector at the LHC, Phys. Lett. B **716**, 1 (2012).
[2] S. Chatrchyan *et al.* (CMS Collaboration), Observation of a new boson at a mass of 125 GeV with the CMS experiment at the LHC, Phys. Lett. B **716**, 30 (2012).
[3] F. Zwicky, Die Rotverschiebung von extragalaktischen Nebeln, Helv. Phys. Acta **6**, 110 (1933).
[4] D. Clowe, M. Bradac, A. H. Gonzalez, M. Markevitch, S. W. Randall, C. Jones, and D. Zaritsky, A direct empirical proof of the existence of dark matter, Astrophys. J. Lett. **648**, L109 (2006).
[5] H. W. Babcock, The rotation of the Andromeda Nebula, Lick Obs. Bull. **498**, 41 (1939).
[6] V. C. Rubin, W. K. Ford, Jr., and N. Thonnard, Rotational properties of 21 SC galaxies with a large range of luminosities and radii, from NGC 4605 (R = 4 kpc) to UGC 2885 (R = 122 kpc)., Astrophys. J. **238**, 471 (1980).
[7] Q. R. Ahmad *et al.* (SNO Collaboration), Direct evidence for neutrino flavor transformation from neutral current interactions in the Sudbury Neutrino Observatory, Phys. Rev. Lett. **89**, 011301 (2002).
[8] Y. Fukuda *et al.* (Super-Kamiokande Collaboration), Evidence for oscillation of atmospheric neutrinos, Phys. Rev. Lett. **81**, 1562 (1998).
[9] P. Langacker, The physics of heavy Z' gauge bosons, Rev. Mod. Phys. **81**, 1199 (2009).
[10] A. Leike, The phenomenology of extra neutral gauge bosons, Phys. Rep. **317**, 143 (1999).
[11] T. G. Rizzo, Z' phenomenology and the LHC, in *Theoretical Advanced Study Institute in Elementary Particle Physics: Exploring New Frontiers Using Colliders and Neutrinos* (2006), pp. 537–575, arXiv:hep-ph/0610104.
[12] R. E. Marshak and R. N. Mohapatra, Quark—lepton symmetry and B-L as the $U(1)$ generator of the electroweak symmetry group, Phys. Lett. **91B**, 222 (1980).
[13] R. N. Mohapatra and R. E. Marshak, Local $B-L$ symmetry of electroweak interactions, majorana neutrinos and neutron oscillations, Phys. Rev. Lett. **44**, 1316 (1980); **44**, 1643(E) (1980).
[14] S. Khalil, Low scale *B*—L extension of the standard model at the LHC, J. Phys. G **35**, 055001 (2008).
[15] P. A. Zyla *et al.* (Particle Data Group), Review of particle physics, Prog. Theor. Exp. Phys. **2020**, 083C01 (2020).
[16] M. Aaboud *et al.* (ATLAS Collaboration), Search for new high-mass phenomena in the dilepton final state using 36 fb^{-1} of proton-proton collision data at $\sqrt{s} = 13$ TeV with the ATLAS detector, J. High Energy Phys. 10 (2017) 182.
[17] A. M. Sirunyan *et al.* (CMS Collaboration), Search for a narrow resonance lighter than 200 GeV decaying to a pair of muons in proton-proton collisions at $\sqrt{s} =$ TeV, Phys. Rev. Lett. **124**, 131802 (2020).
[18] E. ACCOMANDO, D. Becciolini, A. Belyaev, S. De Curtis, D. Dominici, S. F. King, S. Moretti, and C. H. Shepherd-Themistocleous, *W*' and *Z*' searches at the LHC, Proc. Sci. DIS2013 (**2013**) 125.
[19] E. Ma, Verifiable radiative seesaw mechanism of neutrino mass and dark matter, Phys. Rev. D **73**, 077301 (2006).
[20] F. del Aguila, M. Masip, and M. Perez-Victoria, Physical parameters and renormalization of $U(1)^a \times U(1)^b$ models, Nucl. Phys. **B456**, 531 (1995).
[21] P. H. Chankowski, S. Pokorski, and J. Wagner, *Z*-prime and the Appelquist-Carrazzone decoupling, Eur. Phys. J. C **47**, 187 (2006).
[22] J. Chakrabortty, P. Konar, and T. Mondal, Copositive criteria and boundedness of the scalar potential, Phys. Rev. D **89**, 095008 (2014).
[23] B. W. Lee, C. Quigg, and H. B. Thacker, Weak interactions at very high-energies: The role of the Higgs boson mass, Phys. Rev. D **16**, 1519 (1977).
[24] B. W. Lee, C. Quigg, and H. B. Thacker, The strength of weak interactions at very high-energies and the higgs boson mass, Phys. Rev. Lett. **38**, 883 (1977).
[25] M. E. Peskin and T. Takeuchi, Estimation of oblique electroweak corrections, Phys. Rev. D **46**, 381 (1992).
[26] G. Altarelli, R. Barbieri, and F. Caravaglios, The minimal supersymmetric Standard Model and electroweak precision data, Phys. Lett. B **314**, 357 (1993).
[27] M. Baak, J. Cúth, J. Haller, A. Hoecker, R. Kogler, K. Mönig, M. Schott, and J. Stelzer (Gfitter Group Collaboration), The global electroweak fit at NNLO and prospects for the LHC and ILC, Eur. Phys. J. C **74**, 3046 (2014).
[28] A. Arhrib, R. Benbrik, and N. Gaur, $H \to \gamma\gamma$ in inert Higgs doublet model, Phys. Rev. D **85**, 095021 (2012).
[29] R. Barbieri, L. J. Hall, and V. S. Rychkov, Improved naturalness with a heavy Higgs: An alternative road to LHC physics, Phys. Rev. D **74**, 015007 (2006).
[30] J. Haller, A. Hoecker, R. Kogler, K. Mönig, T. Peiffer, and J. Stelzer, Update of the global electroweak fit and constraints on two-Higgs-doublet models, Eur. Phys. J. C **78**, 675 (2018).
[31] A. Joglekar, P. Schwaller, and C. E. M. Wagner, Dark matter and enhanced Higgs to di-photon rate from vector-like leptons, J. High Energy Phys. 12 (2012) 064.
[32] M. A. Arroyo-Ureña, A. Fernández-Téllez, and G. Tavares-Velasco, Flavor changing flavon decay tc at the high luminosity large hadron collider, Rev. Mex. Fis. **69**, 020803 (2023).
[33] M. A. Arroyo-Ureña, A. Chakraborty, J. L. Díaz-Cruz, D. K. Ghosh, N. Khan, and S. Moretti, Flavon signatures at the HL-LHC, Phys. Rev. D **108**, 095026 (2023).
[34] A. Tumasyan *et al.* (CMS Collaboration), Search for invisible decays of the Higgs boson produced via vector boson fusion in proton-proton collisions at s = 13 TeV, Phys. Rev. D **105**, 092007 (2022).
[35] G. Aad *et al.* (ATLAS Collaboration), Measurement of the properties of Higgs boson production at $\sqrt{s} = 13$ TeV in the $H \to \gamma\gamma$ channel using 139 fb^{--1} of pp collision data with the ATLAS experiment, J. High Energy Phys. 07 (2023) 088.
[36] A. Djouadi, The anatomy of electro-weak symmetry breaking. II. The Higgs bosons in the minimal supersymmetric model, Phys. Rep. **459**, 1 (2008).
[37] A. M. Baldini *et al.* (MEG II Collaboration), The design of the MEG II experiment, Eur. Phys. J. C **78**, 380 (2018).
[38] B. Aubert *et al.* (*BABAR* Collaboration), Searches for lepton flavor violation in the decays $\tau^\pm \to e^\pm\gamma$ and $\tau^\pm \to \mu^\pm\gamma$, Phys. Rev. Lett. **104**, 021802 (2010).

[39] D. P. Aguillard *et al.* (Muon g-2 Collaboration), Measurement of the positive muon anomalous magnetic moment to 0.20 ppm, Phys. Rev. Lett. **131**, 161802 (2023).

[40] G. W. Bennett *et al.* (Muon g-2 Collaboration), Final report of the muon E821 anomalous magnetic moment measurement at BNL, Phys. Rev. D **73**, 072003 (2006).

[41] B. Abi *et al.* (Muon g-2 Collaboration), Measurement of the positive muon anomalous magnetic moment to 0.46 ppm, Phys. Rev. Lett. **126**, 141801 (2021).

[42] G. Venanzoni (Muon g-2 Collaboration), New results from the muon $g-2$ experiment, Proc. Sci. EPS-HEP2023 (**2024**) 037 [arXiv:2311.08282].

[43] T. Aoyama *et al.*, The anomalous magnetic moment of the muon in the standard model, Phys. Rep. **887**, 1 (2020).

[44] A. Kurz, T. Liu, P. Marquard, and M. Steinhauser, Hadronic contribution to the muon anomalous magnetic moment to next-to-next-to-leading order, Phys. Lett. B **734**, 144 (2014).

[45] M. Davier, A. Hoecker, B. Malaescu, and Z. Zhang, A new evaluation of the hadronic vacuum polarisation contributions to the muon anomalous magnetic moment and to $\alpha(m_Z^2)$, Eur. Phys. J. C **80**, 241 (2020).

[46] M. Davier, A. Hoecker, B. Malaescu, and Z. Zhang, Reevaluation of the hadronic vacuum polarisation contributions to the standard model predictions of the muon $g-2$ and $\alpha(m_Z^2)$ using newest hadronic cross section data, Eur. Phys. J. C **77**, 827 (2017).

[47] A. Keshavarzi, D. Nomura, and T. Teubner, Muon $g-2$ and $\alpha(M_Z^2)$: A new data-based analysis, Phys. Rev. D **97**, 114025 (2018).

[48] G. Colangelo, M. Hoferichter, and P. Stoffer, Two-pion contribution to hadronic vacuum polarization, J. High Energy Phys. 02 (2019) 006.

[49] M. Hoferichter, B.-L. Hoid, and B. Kubis, Three-pion contribution to hadronic vacuum polarization, J. High Energy Phys. 08 (2019) 137.

[50] A. Keshavarzi, D. Nomura, and T. Teubner, $g-2$ of charged leptons, $\alpha(M_Z^2)$, and the hyperfine splitting of muonium, Phys. Rev. D **101**, 014029 (2020).

[51] T. Blum, N. Christ, M. Hayakawa, T. Izubuchi, L. Jin, C. Jung, and C. Lehner, Hadronic light-by-light scattering contribution to the muon anomalous magnetic moment from lattice QCD, Phys. Rev. Lett. **124**, 132002 (2020).

[52] S. Borsanyi *et al.*, Leading hadronic contribution to the muon magnetic moment from lattice QCD, Nature (London) **593**, 51 (2021).

[53] M. Cè *et al.*, Window observable for the hadronic vacuum polarization contribution to the muon $g-2$ from lattice QCD, Phys. Rev. D **106**, 114502 (2022).

[54] C. Alexandrou *et al.* (Extended Twisted Mass Collaboration), Lattice calculation of the short and intermediate time-distance hadronic vacuum polarization contributions to the muon magnetic moment using twisted-mass fermions, Phys. Rev. D **107**, 074506 (2023).

[55] E.-H. Chao, H. B. Meyer, and J. Parrino, Coordinate-space calculation of the window observable for the hadronic vacuum polarization contribution to $(g-2)\mu$, Phys. Rev. D **107**, 054505 (2023).

[56] F. V. Ignatov *et al.* (CMD-3 Collaboration), Measurement of the $e^+e^- \to \pi^+\pi^-$ cross section from threshold to 1.2 GeV with the CMD-3 detector, Phys. Rev. D **109**, 112002 (2024).

[57] S. M. Barr and A. Zee, Electric dipole moment of the electron and of the neutron, Phys. Rev. Lett. **65**, 21 (1990).

[58] M. Jung and A. Pich, Electric dipole moments in two-Higgs-doublet models, J. High Energy Phys. 04 (2014) 076.

[59] C. Idegawa and E. Senaha, Electron electric dipole moment and electroweak baryogenesis in a complex singlet extension of the Standard Model with degenerate scalars, Phys. Lett. B **848**, 138332 (2024).

[60] V. Andreev *et al.* (ACME Collaboration), Improved limit on the electric dipole moment of the electron, Nature (London) **562**, 355 (2018).

[61] T. S. Roussy *et al.*, An improved bound on the electron's electric dipole moment, Science **381**, adg4084 (2023).

[62] K. Inami *et al.* (Belle Collaboration), Search for the electric dipole moment of the tau lepton, Phys. Lett. B **551**, 16 (2003).

[63] G. W. Bennett *et al.* (Muon (g-2) Collaboration), An improved limit on the muon electric dipole moment, Phys. Rev. D **80**, 052008 (2009).

[64] K. A. Olive (Particle Data Group), Review of particle physics, Chin. Phys. C **38**, 090001 (2014).

[65] I. Esteban, M. C. Gonzalez-Garcia, M. Maltoni, T. Schwetz, and A. Zhou, The fate of hints: Updated global analysis of three-flavor neutrino oscillations, J. High Energy Phys. 09 (2020) 178.

[66] M. C. Gonzalez-Garcia, M. Maltoni, and T. Schwetz, NuFIT: Three-flavour global analyses of neutrino oscillation experiments, Universe **7**, 459 (2021).

[67] N. Aghanim *et al.* (Planck Collaboration), Planck 2018 results. VI. Cosmological parameters, Astron. Astrophys. **641**, A6 (2020).

[68] E. Aprile *et al.* (XENON Collaboration), Dark matter search results from a one ton-year exposure of XENON1T, Phys. Rev. Lett. **121**, 111302 (2018).

[69] J. Aalbers *et al.* (LZ Collaboration), First dark matter search results from the LUX-ZEPLIN (LZ) experiment, Phys. Rev. Lett. **131**, 041002 (2023).

[70] A. Tan *et al.* (PandaX Collaboration), Dark matter search results from the commissioning run of PandaX-II, Phys. Rev. D **93**, 122009 (2016).

[71] A. Alloul, N. D. Christensen, C. Degrande, C. Duhr, and B. Fuks, FeynRules 2.0—A complete toolbox for tree-level phenomenology, Comput. Phys. Commun. **185**, 2250 (2014).

[72] G. Bélanger, F. Boudjema, A. Goudelis, A. Pukhov, and B. Zaldivar, micrOMEGAs5.0: Freeze-in, Comput. Phys. Commun. **231**, 173 (2018).

[73] F. Staub, SARAH 4: A tool for (not only SUSY) model builders, Comput. Phys. Commun. **185**, 1773 (2014).

[74] F. Staub, Exploring new models in all detail with SARAH, Adv. High Energy Phys. **2015**, 840780 (2015).

[75] W. Porod and F. Staub, Spheno 3.1: Extensions including flavour, *CP*-phases and models beyond the MSSM, Comput. Phys. Commun. **183**, 2458 (2012).

[76] L. J. Hall, K. Jedamzik, J. March-Russell, and S. M. West, Freeze-In production of FIMP dark matter, J. High Energy Phys. 03 (2010) 080.

[77] M. Bauer and T. Plehn, *Yet Another Introduction to Dark Matter: The Particle Physics Approach*, Vol. 959 of Lecture Notes in Physics (Springer, New York, 2019), 10.1007/978-3-030-16234-4.
[78] N. Khan and S. Rakshit, Constraints on inert dark matter from the metastability of the electroweak vacuum, Phys. Rev. D **92**, 055006 (2015).
[79] N. Khan and S. Rakshit, Study of electroweak vacuum metastability with a singlet scalar dark matter, Phys. Rev. D **90**, 113008 (2014).
[80] K. Huitu, S. Khalil, H. Okada, and S. K. Rai, Signatures for right-handed neutrinos at the Large Hadron Collider, Phys. Rev. Lett. **101**, 181802 (2008).
[81] K. Das, T. Li, S. Nandi, and S. K. Rai, New signals for vector-like down-type quark in $U(1)$ of E_6, Eur. Phys. J. C **78**, 35 (2018).
[82] B. N. Grossmann, B. McElrath, S. Nandi, and S. K. Rai, Hidden extra $U(1)$ at the electroweak/TeV scale, Phys. Rev. D **82**, 055021 (2010).
[83] W. Abdallah, A. K. Barik, S. K. Rai, and T. Samui, Search for a light Z' at LHC in a neutrinophilic $U(1)$ model, Phys. Rev. D **104**, 095031 (2021).
[84] W. Abdallah, A. K. Barik, S. K. Rai, and T. Samui, Emergent new symmetry from the Higgs shadow, Phys. Rev. D **107**, 015026 (2023).